12-2016

Plasmonic devices based on transparent conducting oxides for near infrared applications

Kim Jongbum
Purdue University

PURDUE UNIVERSITY
GRADUATE SCHOOL
Thesis/Dissertation Acceptance

This is to certify that the thesis/dissertation prepared

By Jongbum Kim

Entitled

Plasmonic Devices Based On Transparent Conducting Oxides for Near Infrared Applications

For the degree of Doctor of Philosophy

Is approved by the final examining committee:

Alexandra Boltasseva
Chair

Alexander V. Kildishev

Minghao Qi

Vladimir M. Shalaev

To the best of my knowledge and as understood by the student in the Thesis/Dissertation Agreement, Publication Delay, and Certification Disclaimer (Graduate School Form 32), this thesis/dissertation adheres to the provisions of Purdue University's "Policy of Integrity in Research" and the use of copyright material.

Approved by Major Professor(s): Alexandra Boltasseva

Approved by: Venkataramanan Balakrishnan 11/16/2016

Head of the Departmental Graduate Program Date

PLASMONIC DEVICES BASED ON TRANSPARENT CONDUCTING OXIDES FOR NEAR INFRARED APPLICATIONS

A Dissertation

Submitted to the Faculty

of

Purdue University

by

Jongbum Kim

In Partial Fulfillment of the

Requirements for the Degree

of

Doctor of Philosophy

December 2016

Purdue University

West Lafayette, Indiana

To my parents, brother and my beloved family, Hyeryung and Ganyu

ACKNOWLEDGMENTS

First and foremost, I would like to thank my advisor, Prof. Alexandra Boltasseva, for her great care and effort throughout my life in Purdue. Under her tutelage and continuous guidance, I have learned the insight on optics and encouraged to be a good researcher. I would also like to thank Prof. Vladimir Shalaev for being an supportive and inspiring advisor. I am grateful to Prof. Alexander Kildishev for his helpful friendly suggestions. I extend my gratitude to Prof. Minghao Qi for helpful discussions, especially when I was MS student.

The research in this dissertation would not have been possible without constant supports from collaborating groups. I thank Prof. Nader Engheta, Dr. Joshua Caldwell, Prof. Andrea Alu, Prof. Hossein Mosallaei, and Prof. Vladimir I. Gavrilenko for fruitful collaborations. I would like to express my sincere gratitude to the entire colleagues in our research group who provided a pleasant working environment.

The most important people I need to thank are my parents. They have been very patient and supportive throughout my study. It is apparent that without their support, I would not have been able to pursue my goal and dream in my life. Finally, I would like to express my gratitude to my wife who have always believed and encouraged me.

TABLE OF CONTENTS

Page

Page

LIST OF TABLES

LIST OF FIGURES

Figure Page

Figure Page

SYMBOLS

m	mass
v	velocity
ε'	Real part of permittivity
ε''	Imaginary part of permittivity
ω_p	Plasma frequency
γ	Drude-damping co-efficient
eV	electron-volt (1 eV = 1.602 10^{19}) J
$sccm$	standard cubic centimeter per minute (1 $sccm$ = 16.67 standard mm^3/s)
$Torr$	pressure (1 $Torr$ = 133.28 Pa)

ABBREVIATIONS

AFM	Atomic Force Microscope
TCO	Transparent Conducting Oxide
LSPR	Localized Surface Plasmon Resonance
GSPR	Gap Surface Plasmon Resonance
IR	Infrared
NIR	Near Infrared
MIR	Mid Infrared
SEM	Scanning Electron Microscope
SPP	Surface Plasmon Polariton
AZO	Aluminum Doped Zinc Oxide
GZO	Gallium Doped Zinc Oxide
ITO	Tin Doped Indium Oxide
FIB	Focused Ion Beam
EDS	Energy Dispersive X-Ray Spectroscopy
ENZ	Epsilon Near Zero
STEM	Scanning Transmission Electron Microscope
TO	Transformation Optics
PLD	Pulsed Laser Depostion
SPR	Surface Plasmon Resonance
QWP	Quarter Wave Plate
SEIRA	Surface Enhanced Infrared Absorption
MIM	Metal-Dielectric-Metal
ODT	Octadecanethiol
HSQ	Hydrogen Silsesquioxane

ABSTRACT

Kim, Jongbum PhD, Purdue University, December 2016. Plasmonic Devices Based On Transparent Conducting Oxides For Near Infrared Applications . Major Professor: Alexandra Boltasseva.

In the past decade, there have been many breakthroughs in the field of plasmonics and nanophotonics that have enabled optical devices with unprecedented functionalities. Even though remarkable demonstrations of nano-photonic devices have been reported, constituent materials are limited to the noble metals such as gold (Au) and silver (Ag) due to their abundance of free electrons which enable the support of plasmon resonances in the visible range. With the strong demand for extension of the optical range of plasmonic applications, it is now a necessity to explore and develop alternative materials which can overcome intrinsic issues of noble metals such as integration challenges, considerable optical losses, and lack of tunability of their optical properties. As most promising alternative to noble metals, transparent conducting oxides (TCOs) have been proposed as a new class of plasmonic materials for the infrared (IR) applications. The main objective of this thesis is to explore the various plasmonic devices based on TCOs and to evaluate the capabilities of TCOs as alternative metallic component for plasmonic system. In this thesis, a brief discussion of the general (optical, electrical and morphological) properties of several types of metal oxides is provided in the introduction, and I describe the demonstrations of various plasmonic devices such as plasmonic resonator for bio-sensing and waveplate metasurfaces. Next, I explain about the role of TCOs as epsilon-near-zero (ENZ) substrate with experimental study on the impact of TCOs to local resonator. In conclusion, the technological importance of the IR range is apparent and growing, and as plasmonics develops a niche at these frequencies, I believe this study represents a scientific directive toward the quest to bring plasmonics into the IR.

1. INTRODUCTION

1.1 Limitation of Noble Metals

Plasmonics exploit the interaction between electromagnetic field and free electrons in a metal [1–5]. Free electrons in the metal can be excited by the electric component of light to have collective oscillations. The coupled oscillations called as surface plasmons (SPs) can propagate at the planar surface between metal and dielectric, or they can strongly localize at the surface of subwavelength nanostructures [2, 6, 7]. These novel concepts has evolved into a broad field of nanoscale optics with the development of optical devices with unprecedented functionalities such as nanoantennas for optical detector and sensor [8], hyperbolic-metamaterials (HMMs) including hyperlens [9, 10], flat photonics for wavefront engineering such as planar lens [11, 12], and optical waveguides [13] and modulator [14]. The performance of such plasmonic devices highly depends on the geometry and optical properties of the constituent materials. For a design of plasmonic device, geometry has to be optimized to obtain the required functionality, and specific type of noble metals have been chosen as plasmonic materials. As for the choice of plasmonic component, noble metals suffer from several drawbacks which prevent the realization of practical nanophotonic devices [15–17]. First of all, optical loss is inevitable in the visible and ultra-violet (UV) spectral ranges, arising in part from interband electronic transitions. Especially, high optical loss in infrared (IR) range have prevented some of the promising applications from being realized. Optical loss can be additionally increased when these materials are grown as thin film. Metal thin films pose quite different morphologies in comparison with bulk metal, and many small grains introduce additional grain-boundary scattering for free electron and in turn increase the losses. Furthermore, additional losses can arise from the nanopatterning of noble metals. Experimental value of optical losses from nanopatterned metal film has 3 to 5 times larger than losses of thin film [18].

Another limitation of noble metals is that optical properties cannot be easily adjustable or tunable [19]. The carrier concentration of metals cannot be changed much with the external force as like electric fields, optical fields, or temperature. Therefore, in applications where switching or modulation of the optical properties is essential, noble metals are not the suitable choices. Another drawback, especially for transformation optics (TO) [20] is that a negative real part of permittivity that is too large in the infrared (IR) range including telecommunication wavelength of 1.55 m. Large negative values of real permittivity limit the realization of TO devices because such devices require similar magnitudes of for their metallic and dielectric components. Dielectrics at optical frequencies have permittivity values on the order of 1, while for metals it is on the order of 10 or more. Thus, conventional metals are typically not good choices for many TO-based applications.

As well as high optical losses and not compatibility of TO applications, there are technological challenge to integrate noble metal into nanoelectronic and nanophontonic device. These metals can diffuse into silicon to form deep traps, which severely affects the performance of nanoelectronics devices. Hence the integration of noble metals into silicon manufacturing processes is a difficult challenge. In addition, growth of smooth thin film of noble metal is also challenge, so it diminishes the possibility to scale down the plasmonic device with desired performance.

1.2 Alternative Plasmonic Materials

Considering the constraints of noble metals for plamsonic applications, it is obvious that alternative plasmonic materials must be developed for practical applications of nanophotonics systems [21–23]. The integration of new materials not only opens up possibilities for new devices, but it also significantly improves the performance of many existing plasmonic devices. It may be noted that smaller optical loss does not necessarily mean better performance of a plasmonic device. In general, the device performance depends on both the real and imaginary parts of permittivity. Therefore, both the loss and the real part of the permittivity are critical factors to consider when developing alternative plasmonic materials. In Fig. 1.1, various materials are

classified on the basis of two important parameters that determine the optical properties of conducting materials: the carrier density and carrier mobility. Higher carrier mobilities translate to lower material losses.

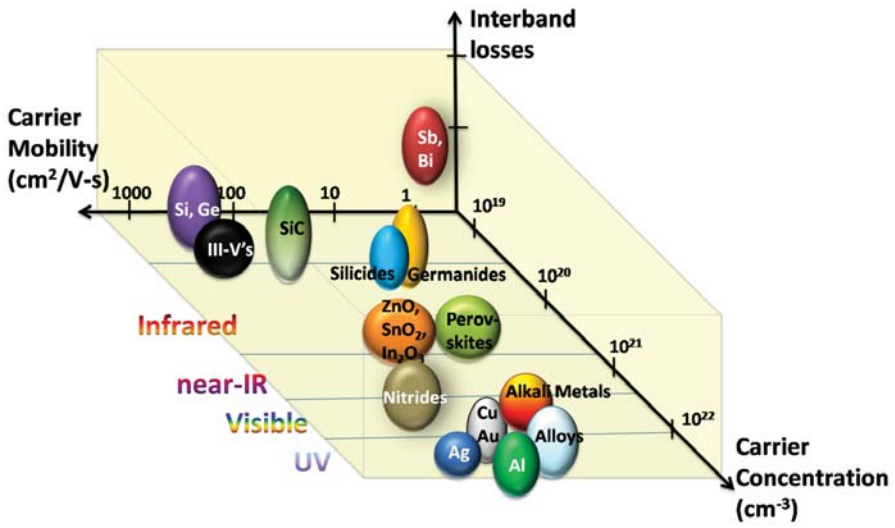

Fig. 1.1. Carrier concentration (maximum doping concentration for semiconductors), carrier mobility, and interband losses for various type of materials such as noble metals (Al, Ag, Cu and Au), Semiconductors (Silicon, Germanium, and Silicon Carbide), alkali metals and intermetallics (silicides, germanides, borides, nitrides, oxides, and metallic alloys). Spherical bubbles represent materials with low interband losses, and elliptical bubbles represent those with larger interband losses in the corresponding part of the electromagnetic spectrum.

1.3 Transparent Conducting Oxides

As shown in Fig. 1.1, transparent conducting oxides (TCOs) has been proposed as alternatives to noble metals in the IR regimes [15, 24]. Oxide semiconductors such as zinc oxide, cadmium oxide and indium oxide can be highly doped to make them conducting films [25, 26]. Since these semiconductors have a large bandgap, they are transparent in the visible range. Hence, these materials are widely used as conducting electrodes in the display panel [27] and solar cell where the lights are required to transmit through the devices. One of the most popular TCOs is indium tin oxide (ITO) [28] due to its thermal and chemical stability. However ITO is becoming

more expensive due to high market demand. For this reason, doped semiconductor such as aluminum or gallium doped zinc-oxide (AZO or GZO) have been considered as alternative to ITO in the industry. Aluminum and Zinc are very common and inexpensive materials, hence, considering the fact that the primary goal of this study is to search industry-friendly and practical plasmonic materials, it is necessary to study doped zinc oxide as promising alternatives. Similar with ITO, AZO and GZO can be doped very heavily, and then exhibit high DC conductivity which gives them metal-like optical properties in the NIR range. Similar with any other semiconductor, the optical properties of these materials can be tuned by changing the carrier concentration/doping. They can be grown into thin films and many different nanostructures, polycrystalline and crystalline structures, patterned by standard fabrication procedures and integrated with many other standard technologies. Thus, TCOs can provide extraordinary tuning and modulation of their complex refractive index because their carrier concentrations can be changed by orders of magnitude by applying an electric field. Such materials can go from being metallic to dielectric, opening up exciting possibilities for novel device concepts.

1.4 Outline of Dissertation

The major challenge of this study at the starting point is to achieve the carrier concentration of TCOs high enough to provide a negative real permittivity in NIR range, especially at the telecommunication wavelength (1.55 μm) with the relatively low losses comparable smaller than noble metals. For the understanding of these materials to optimize the optical properties, chapter 2 provides the background information on optical characteristics of TCOs. As an extension of study on optical properties of TCOs, chapter 3 outlines the collaboration work on theoretical study on TCOs with First Principle Theory. The next objective of this work will focus on the capability of TCOs for the potential and novel concept design of optical devices. Chapter 4 begins with discussing the fabrication technique to realize nano-scale nanostructure of TCOs. By employing the conventional standard nanofabrication methods, circular shape of nanostructure is fabricated to explore

the plasmonic properties of TCOs by detecting localized surface plasmon resonance (LSPR) of nanopatterned TCOs. In the chapter 5, the study of resonance behavior of TCOs extends from single layer nanostructure to multilayer nanostructure, which enables to excite the gap surface plasmon resonance in the dielectric layer between two metal layers. It demonstrates the versatility of resonator design operating at IR frequencies for sensing applications. Chapter 6 presents a design of QWP metasurface which can change linearly polarized light to circularly polarized light. Chapter 7 discusses the gold antenna behavior on ENZ substrate. Thick layer of TCOs are used for ENZ substrate in NIR range. The unusual behavior of antenna is demonstrated by lying on the ENZ substrate. Finally, chapter 8 gives a conclusion and a plan for future work.

2. FUNDAMETNAL CHARACTERISTICS OF TRANSPARENT CONDUCTING OXIDES FOR PLASMONIC MATERIALS IN THE INFRARED

2.1 Sample Prepration

Thin films of TCOs can be deposited by many physical-vapor and chemical-vapor deposition techniques. Among the various deposition technique, we employ pulsed-laser-deposition (PLD) [29] which is a laser-based technique used to grow high quality thin films of complex materials on substrates. A target is vaporized by short and intense laser pulses and forms a plasma plume Our system uses a KrF excimer laser (Lambda Physik GmbH) at a wavelength of 248 nm for source material ablation. The chosen ablation targets were Ga_2O_3 and ZnO for GZO, Al_2O_3 and ZnO for AZO and In_2O_3 and SnO_2 for ITO. The targets were purchased from the Kurt J. Lesker Corp. with purities of 99.99% or higher. The required composition of the deposited film was achieved by alternating the laser ablation over two different targets with an appropriate number of pulses on each target. A single cycle consisting of a few laser pulses on each target was repeated many times until the desired film thickness was achieved. The number of pulses in each cycle was designed to be small enough so that the effective layer thickness deposited in a single cycle can be less than a few atomic layers, resulting a homogeneous mixture of the constituent materials in the final film. For example, the typical deposition parameters for 1 wt% gallium and aluminum doping are listed in Table 2.1.

To achieve the high carrier concentration of TCOs, the temperature and the oxygen should be optimized at the level lower than conventional conditions. In general, high temperature (above 250^oC) and high oxygen pressure (above 5 mTorr) is suggested as optimal conditions for deposition of good electrode because small plasma frequency allows to have high transmission in visible range. From the several step of optimization, our films pose the highest carrier concentration when the films

Table 2.1.
Typical deposition parameters for 1 wt% for AZO and GZO

Dopant	Al (AZO)	Ga (GZO)	Sn (ITO)
Ratio of Pulses	120 : 1	180 : 1	200 : 1
Ablation rate(Hz)	1	1	1
Oxygen partial pressure (Torr)	10^{-3}	10^{-3}	10^{-3}

were grown in an oxygen ambient with an oxygen partial pressure of 0.4 mTorr (0.053 Pa) or lower and the substrate was heated to temperatures around 50-100 ^{0}C during deposition. The high concentration can be ascribed by intrinsic defects such as oxygen vacancies (VO) contributing two electrons.

2.2 Optical Properties of TCOs

The material's complex electrical permittivity or dielectric function can describe the interaction between incident electromagnetic waves and materials. The real part of the dielectric function represent the strength of the polarization induced by an external electric field, and the imaginary part of the dielectric function describes the optical losses encountered in polarizing the material. Loss mechanisms in the optical frequencies can be arisen from intraband effects, interband effects and lattice vibrations known as phonon interactions [30]. Losses due to intraband contributions primarily arise from conduction-band electrons. Because the conduction electrons have a near continuum of available states, their interaction with an electromagnetic field is well described by Drude theory [31], where conduction electrons are treated as a 3-D free-electron gas.

$$\varepsilon(\omega) = \varepsilon(\omega)' + i\varepsilon(\omega)'' = \varepsilon_b - \frac{\omega_p^2}{\omega^2 + \gamma^2} + i\frac{\omega_p^2\gamma}{(\omega^2 + \gamma^2)\omega} \tag{2.1}$$

$$\omega_p^2 = \frac{ne^2}{\varepsilon_0 m^*} \tag{2.2}$$

where ϵ_b is the polarization response from the core electrons (background permittivity), ϵ_p is the plasma frequency and γ is the Drude relaxation rate. For the equation of plasma frequency (ω_p^2), n is the conduction electron density, and m^* is the effective optical mass of the conduction electrons. In general, $_b$ depends on wavelength (which is typically accounted by including the Lorentz oscillators terms) but for some spectral ranges it can be roughly approximated as constant. Because plasmonic applications require materials with negative real part of permittivity, it is noted that plasma frequency in Eq. 2.2 has to be larger than the desired frequency of application. As referred to γ, significant losses occur when free electron in conduction band absorbs an incident photon and jump to higher, empty energy levels.

In semiconductors and insulators, valence electrons absorbing the energy from a photon shift into the conduction band, resulting in loss [32]. This loss mechanism induces the increase of the imaginary part of permittivity and such phenomenon can be described by Lorentz oscillator model. The two-level description of the absorption process results in a simple Lorentz model as shown in the Eq.2.3.

$$\varepsilon(\omega) = \varepsilon_b + \frac{\omega_{p,12}^2}{\omega_{12}^2 - \omega^2 - 2i\omega\gamma_{12}} \tag{2.3}$$

where ω_{12} is the energy difference between levels 2 and 1, γ_{12} is the damping coefficient of the resonance, and $\omega_{p,12}$ is the strength of the resonance. When there are many of such interacting energy levels, the effective permittivity can be expressed as a summation over all allowed Lorentzian terms. This is a popular approach utilized in the Drude-Lorentz model to reasonably approximate the dielectric function of metals. Optical response from the bound electrons can be also described by the oscillator model containing a set of Gaussian type single oscillators. Due to structural disorder in solid alloys, the optical functions contain a random component of optical response well described by a Gaussian distribution. The following equation presents the Gaussian oscillator model:

$$\varepsilon_{gaussian}(\omega_m, \sigma_m) = \varepsilon_{m1} + i\varepsilon_{m2} \tag{2.4}$$

$$\varepsilon_{m1} = \frac{2}{\pi} P \int_0^{\infty} \frac{\xi \varepsilon_{m2}(\xi)}{\xi^2 - \omega^2} d\xi \tag{2.5}$$

$$\varepsilon_{m2} = A_m e^{-\frac{(\omega-\omega_m)^2}{\sigma_m}} + A_m e^{-\frac{(\omega+\omega_m)^2}{\sigma_m}} (\sigma_m = \frac{\Gamma_m}{2\sqrt{ln(2)}}) \tag{2.6}$$

where ε_∞ is the macroscopic dielectric permittivity, A_m is proportional to the oscillator strength, ω_m is the central frequency of interband electronic transitions represented by the Gaussian oscillator, and Γ_m is the broadening of the Gaussian oscillator. The total plasmonic effect at optical frequencies is thus most accurately modeled by combining both the free-electron and bound-electron contributions in the form of the Lorentz-Drude model or Gaussian-Drude model.

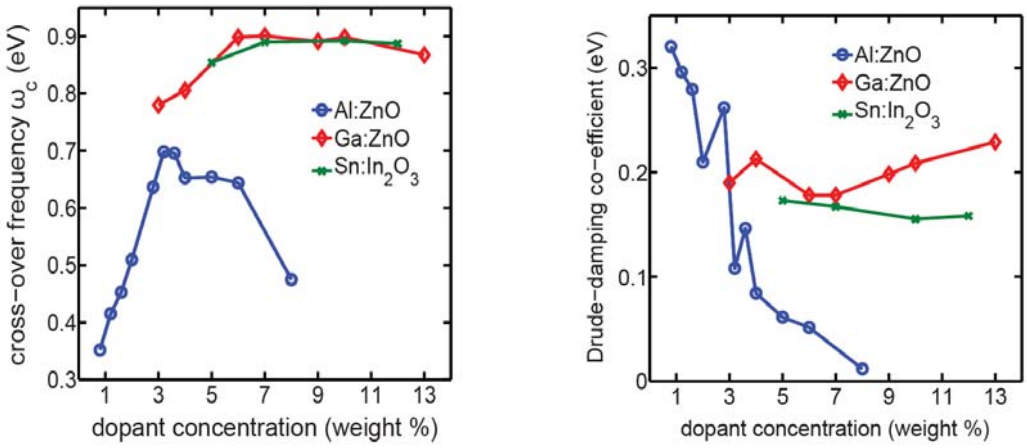

Fig. 2.1. Left panel: Cross-over frequency (frequency at which real permittivity crosses zero) of Al:ZnO, ITO and Ga:ZnO films as a function of dopant concentration. Right panel: Drude-damping coefficient (γ) vs. dopant concentration. The films were deposited at 100 ^{0}C (AZO and ITO) and 50 ^{0}C (GZO) with oxygen partial pressures of 0.4 mTorr. The ablation energy was about 2 J/cm^2.

The optimization curves for GZO, ITO and AZO are shown in Fig. 2.1. The optical characterization of the thin films was performed using a spectroscopic ellipsometer (V-VASE, J. A. Woollam). The dielectric function was retrieved by fitting a Drude+Lorentz oscillator model to the ellipsometry data. The cross-over frequency (ω_c) is defined as the frequency at which the real permittivity of the material crosses

zero. Since ω_c is directly proportional to plasma frequency (ω_p) and ω_p is proportional to the square of carrier concentration, Fig. 2.1 depicts the carrier concentration trend as a function of film composition. While the highest cross-over frequency achieved for AZO is about 0.7 eV, the same for GZO and ITO is around 0.9 eV [33]. The substrate temperature and oxygen partial pressure during deposition of these films play significant roles in achieving the highest possible carrier concentration. The optimum values were found to be close to the parameters used in the data for Fig. 2.1.

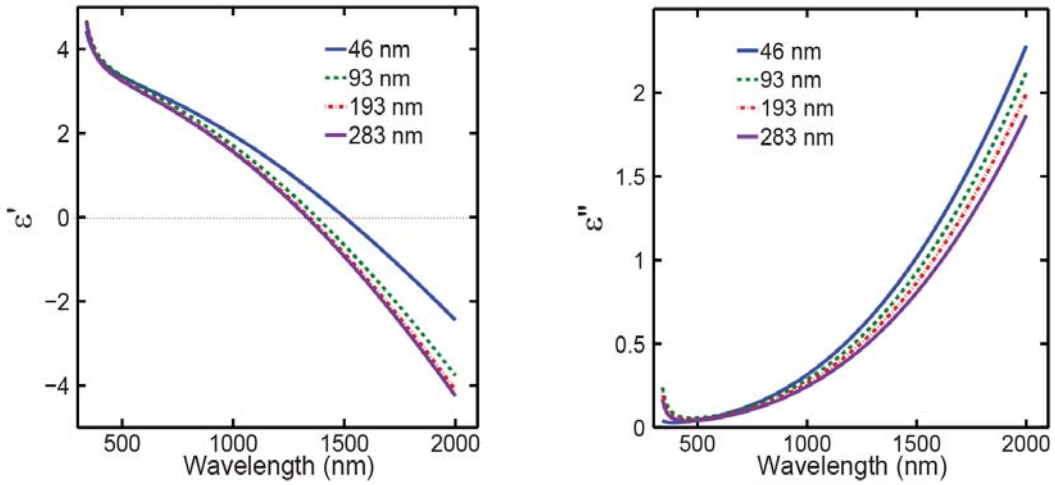

Fig. 2.2. Optical properties of GZO thin films with different thicknesses deposited on glass substrates. The films were deposited under identical conditions except for the duration of deposition.

Owing to their non-stoichiometric nature, TCO films are known to exhibit thickness-dependent properties [34]. This is because the interface with the substrate can have many carrier trap states, and hence the net carrier concentration in the film depends on the thickness (volume to surface ratio) of the film. In many nanoplasmonic devices, thin film structures are used as building blocks, and therefore it is necessary to understand how the optical properties of TCO thin films depend on their thickness. We have studied the thickness-dependent optical properties of GZO thin films on glass substrates. Figure 2.2 shows the dielectric function of GZO films with different

thicknesses. The films with thicknesses greater than about 50 nm exhibit very little thickness dependence in their optical properties.

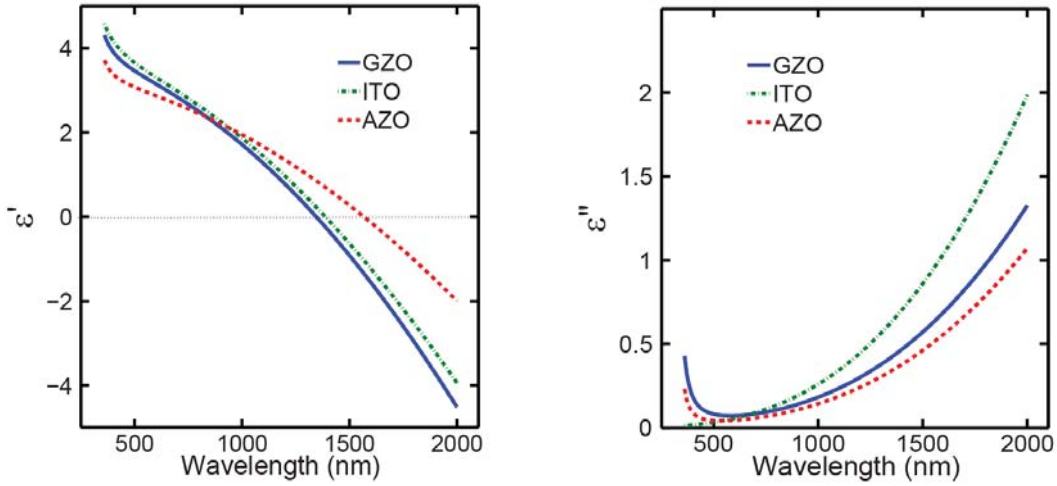

Fig. 2.3. Comparison of the optical properties of pulsed laser deposited TCO films with the smallest cross-over wavelengths. The films were deposited onto glass substrates at 100 ^0C (AZO and ITO) and 50 ^{0}C (GZO) with oxygen partial pressures of 0.4 mTorr.

As a comparison of the three different TCOs in our study, in Fig. 2.3 we plot the optical properties of AZO, GZO and ITO films. The plots correspond to the TCO films with the lowest cross-over wavelengths and lowest losses. Notably, AZO offers the lowest Drude damping, but it also has the lowest ω_c (and hence the longest cross-over wavelength). GZO and ITO can produce cross-over wavelength as low as 1.2 μm. However, Drude damping in GZO is slightly higher than that in AZO and lower than that in ITO.

2.3 Surface Plasmon Polaritons on TCOs

Surface plasmon polaritons are propagating charge-density waves on metaldielectric interface that can be excited by attenuated total reflection of an incident electromagnetic wave. SPP excitation on TCO films was used to verify the applicability of these materials for NIR plasmonic devices, especially at the telecommunication wavelength of 1.55 μm [35–37]. We used a prism coupler (Metricon 2010/M) and

implemented a KretschmannRaether configuration for SPP coupling (see Fig. 2.4). The TCO thin films were directly deposited on BK7 glass coupling prisms (n = 1.501), and the thicknesses of AZO, GZO and ITO were 154 nm, 147 nm and 139 nm, respectively.

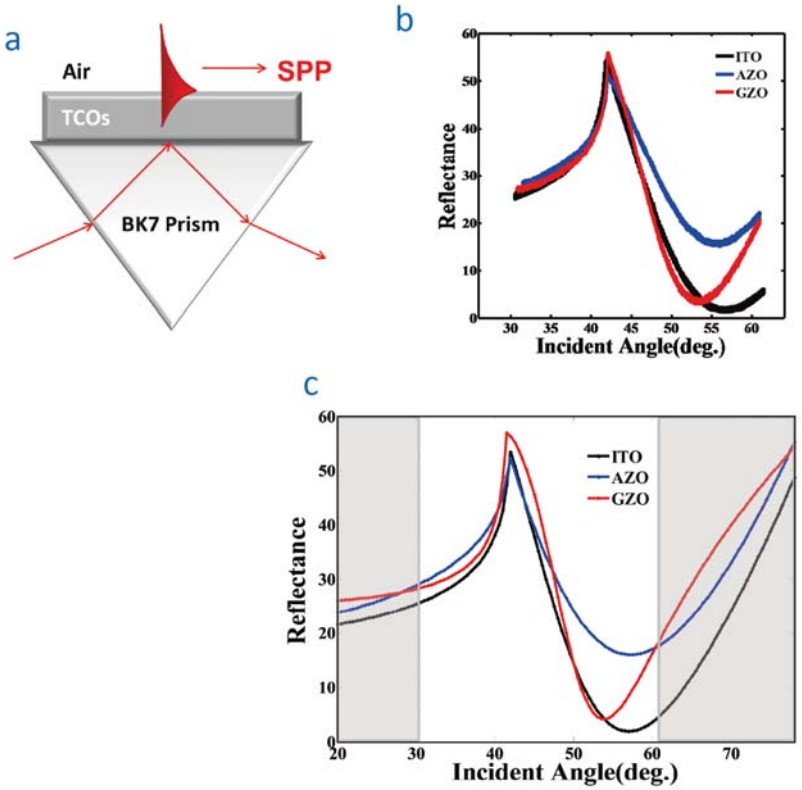

Fig. 2.4. (a) Schematic view of the experimental setup for SPP excitation in attenuated total reflection. (b) Reflectance curve vs. incident angle of light with 1.55 μm wavelength for ITO, AZO and GZO. (c) Simulation of reflectance curve vs. incident angle of light with 1.55 μm wavelength for ITO, AZO, and GZO.

A beam of TM-polarized, monochromatic laser at a wave-length of 1.55 μm was used to illuminate the sample through the input facet of the 45^o BK7 glass coupling prism. While rotating the sample with respect to the laser beam, the far-field reflectance was measured with a detector. This provided a measurement of the reflected intensity for a range of internal angles from 30^o to 62^o. Theoretically, SPPs at a TCO-air interface are expected in wavelength region where the real part of the TCO permittivity (TCO) is less than 1. The experimental observation of broad SPP

resonances in ITO films was previously reported in [36]. Those reports demonstrated a thickness-dependent SPP on ITO thin films. AZO was previously reported to be incapable of supporting SPPs at 1.55 μm because of its smaller plasma frequency. However, the AZO films are optimized for large plasma frequencies at 1.55 μm. The experimental data from the prism coupling reflectance measurements clearly shows the SPP existence on AZO films at a wavelength of 1.55 μm (Fig. 2.4(b)). The reflectance measurements from the prism coupler were verified using analytic calculations. Fig. 2.4(c) shows the calculated reflectance values for AZO, GZO and ITO thin films. The dip in reflectance occurring around 50-60 corresponds to the excitation of SPPs on these films.

2.4 Comparative Study

Based on the anlysis of properties of TCOs, especially AZO and GZO, finding a plasmonic or metamaterial application where these materials can outperform the conventional metals is necessary to design the outstanding optical device with proposed alternative materials. As we emphasized several times, the major advantage of TCOs is the low optical loss. Figure 2.5 plots the optical loss or imaginary permittivity (ϵ'') of AZO, GZO and ITO along with those of noble metals, gold and silver.

However, it may be noted that smaller imaginary permittivity or optical loss does not necessarily mean better performance of a plasmonic or metamaterial device. In general, the device performance depends on both the real and imaginary parts of permittivity. The performance of plasmonic devices can be quantified based on the figure-of-merit (FoM) which forms a common platform to evaluate the performance of various materials used in different applications over a wide frequency band. Adopting the general FoM definition for localized surface-plasmon resonance (LSPR) applications as $|Re(\epsilon)|/\sqrt{Im(\epsilon)}$, the efficiency of various plasmonic materials can be evaluated [15]. The same FoM holds good for any of the SPP waveguiding applications as well. Figure 2.6 plots this quantity for GZO, gold and silver. Gener-

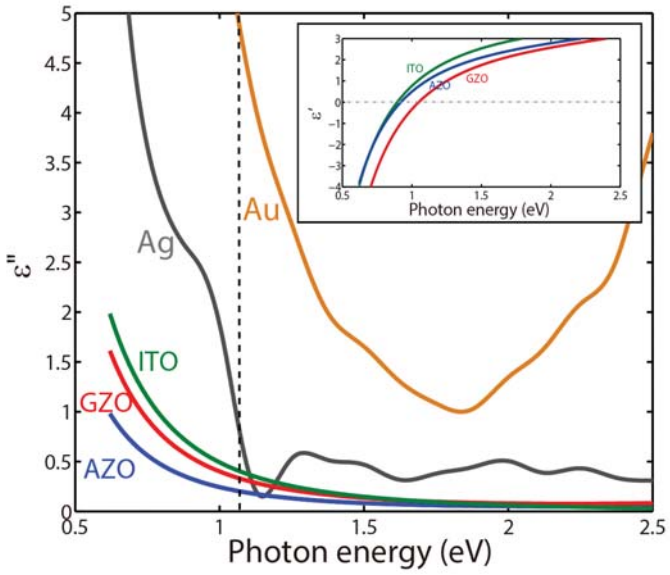

Fig. 2.5. Optical loss or imaginary part of permittivity of three transparent conducting oxides: indium tin oxide (ITO), Al-doped ZnO (AZO) and Ga-doped ZnO (GZO) compared with that of gold and silver. Optical constants of thin films of AZO, GZO and ITO are from reference [35] and those of gold and silver are from reference [19]. The inset shows the real part of permittivity of AZO, GZO and ITO. The vertical dashed line corresponds to the photon energy where real permittivity of GZO crosses zero.

ally speaking, gold and silver outperform TCOs for these applications. Nevertheless, TCOs are good alternatives in the NIR for simple device geometries [16].

Figure 2.6 also plots the FoM for transformation optics (TO) devices which can be defined as the ratio of the real part of the refractive index (n') to the imaginary part (n''). From this plot, we can clearly notice that TCOs are promising candidates as plasmonic materials in the NIR for non-resonant applications such as TO devices. Devices such as epsilon-near-zero and hyperbolic metamaterials do benefit significantly by using TCOs as their plasmonic components. One of these conditions is that the real part of permittivity of the metallic and dielectric components should be nearly the same magnitude [38]. In the visible and near-IR frequencies, this condition is not sufficiently met by conventional metals. However, TCOs do meet this condition in NIR wavelength range. Considering the tunability of optical properties and zero-crossing real permittivity in NIR wavelength, TCOs are promis-

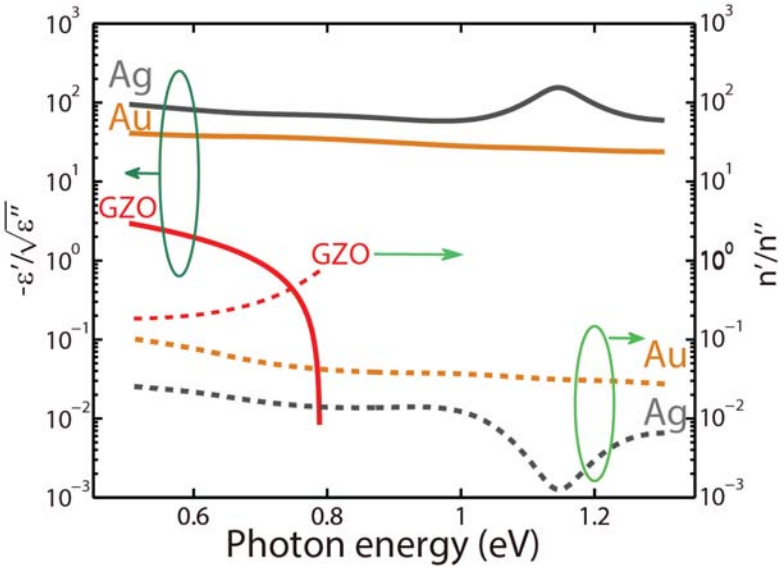

Fig. 2.6. Figure-of-merit (FoM) of localized-surface plasmon resonance (LSPR) and SPP waveguiding devices (solid lines) and transformation optics (TO) devices (dashed lines) calculated for Ga-doped ZnO (GZO), gold and silver as plasmonic materials.

ing candidates as plasmonic materials in the near-infrared and longer wavelengths for devices based on epsilon-near-zero (ENZ), hyperbolic metamaterials, localized surface-plasmon resonance and tunable devices.

An additional advantage of TCOs lies in their ease of fabrication and integration. Fabrication techniques such as chemical vapor deposition, atomic layer deposition and molecular beam epitaxy can be employed to produce oxide films of high quality. Furthermore, employing lattice-matched systems allows hetero-epitaxy, which could produce high-performance, monolithic devices. For example, AZO and GZO on sapphire or ZnO substrates could result in superlattice/monolithic devices [39, 40]. It is important to note that conventional metals such as gold and silver are not compatible with standard CMOS processes.

3. FIRST PRINCIPLES DENSITY FUNCTIONAL THEORY FOR OPTICAL PROPERTIES OF GALLIUM DOPED ZINC OXIDE

3.1 Motivation

To understand a doping mechanism in TCOs, we use electronic bandstructure calculations to study the optical properties of GZO. The optical properties of heavily doped GZO possess non-trivial dependence on the doping concentration, especially when doped as high as close to the solid-solubility limit. Though there are many reports studying the electronic or optical properties of heavily doped GZO films, it is not well understood the relation between the carrier concentration, crystallinity of films, and alloying effects with the optical properties. Therefore, first principles density functional theory (DFT) has been employed to study the influence of each of these factors on the optical properties of plasmonic GZO films. Theoretical studies are supported with experimental studies on n-type wurtzite GZO poly-crystalline films. First principles DFT calculations are incorporated to study the electron energy structure and optical functions of heavy GZO crystals. The ground states of the systems are obtained by the total energy minimization method within the local density approximation (LDA). The effects of Ga doping on the electron energy structure and optical functions are presented.

3.2 Experimental Characterizations

To probe the dependence of the optical properties and band structure of the GZO films on the doping concentration, The Ga_2O_3 doping concentration was varied in the range from 0 to 6 weight%. The dependence of the optical properties of the GZO films on the doping concentration was studied in the spectral region from 0.73 to

6.52 eV. In this work, we used the Gaussian oscillator model which is described in previous section. The retrieved parameters are listed in the Table 3.1.

Table 3.1.
Extracted Drude+Gaussian oscillator parameter

Doping rate	Undoped	3wt%	6wt%
ε_∞	2.812	2.557	2.439
ω_p	0	1.508	1.901
Γ_p	-	0.159	0.092
A_1	1.742	1.630	1.427
A_2	1.865	2.101	1.676
Γ_1	0.596	1.036	0.764
Γ_2	3.222	2.922	3.251
ω_1	3.611	4.335	4.371
ω_2	5.905	6.603	5.825

The optical band gap in GZO films can be determined from the spectral dependence of the absorption coefficient (α). In the direct-gap semiconductors such as ZnO, the absorption co-efficient α and optical bandgap (E_g) are related by Eq.3.1 [41]:

$$\alpha\hbar\omega = A(\hbar\omega - E_g)^{\frac{1}{2}} \tag{3.1}$$

where, $\hbar\omega$ is the incident photon energy and A is a proportionality constant. The values of E_g are extracted from the plot of α^2 vs. $\hbar\omega$ as shown in Fig. 3.1. The E_g values are obtained from the intercept of the α^2 asymptote on the horizontal axis. This procedure results in values of E_g of 3.25 eV for undoped ZnO, 3.66 eV, and 3.89 eV for 3wt % and 6wt % GZO films respectively.

The structural properties of ZnO and GZO thin films were examined using X-ray diffraction (Panalytical X'Pert Pro MRD) studies with a parallel beam configuration and CuKα excitation. Each crystalline semiconductor has a unique XRD pattern to identify its crystal structure. When X-ray light with a wavelength λ is incident on a crystal, a diffraction peak occurs if the Bragg condition is satisfied the equation 3.2.

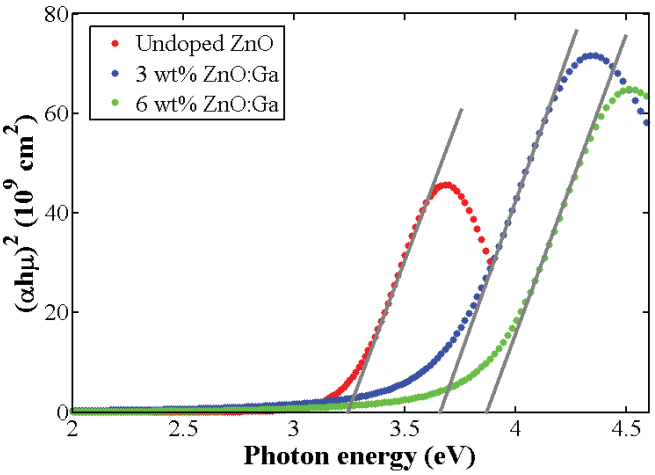

Fig. 3.1. Square of the absorption coefficient as a function of photon energy for ZnO, 3wt% GZO and 6wt% GZO thin films. E_g proportional to $(\alpha\hbar\omega)^2$ is calculated by fitting linear line to spectra E_g (Undoped ZnO):3.25 eV, E_g (3 wt% GZO):3.66 eV and E_g (6 wt% GZO):3.25 eV

$$n\lambda = 2d\sin\theta \tag{3.2}$$

where d is the lattice spacing of the crystal and is the angle of incidence. The CuK emission ($\lambda = 1.5418$ A) from a copper target is the most common X-ray source for the diffraction measurement. Figure 3.2 shows X-ray diffraction data ($\omega - 2\theta$ scans) of the films with different concentrations of gallium (undoped, 3 wt% and 6 wt%). The GZO-films deposited are polycrystalline and strongly oriented along the c-axis normal to the quartz substrate surface. Strong orientation of grains resulted in 002 reflection appearing around 34.5° as the only dominant peak observed [42]. In this work, only 002 reflection peak is considered for subsequent analyses (see Fig. 3.2).

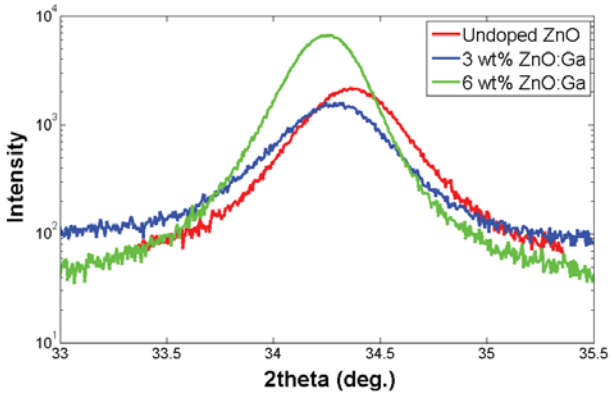

Fig. 3.2. X-Ray diffraction ($\omega-2\theta$) patterns for ZnO, 3wt% GZO and 6wt% GZO thin films. The peak shown in the figure corresponds to 002 reflection.

XRD pattern can be used to determine the grain size of thin film by calculating the full width half maximum (FWHM) of diffraction peak. The FWHM of diffraction peak becomes much narrower and sharper as increasing the doping concentration, referring that the crystallinity of ZnO thin film is improved. This result correspond to the reduction of optical loss of GZO thin film as we increase the doping rate because of the decrease of grain boundary and electron scattering.

3.3 Theoretical Methods

Heavy Ga-doped wurtzite ZnO crystals are modeled by the first principles pseudopotential theory using super-cell method. Equilibrium atomic structures of w-GZO are obtained from the total energy minimization method within DFT using *ab initio* pseudopotentials [43]. We employ the super-cell approach to model the substitutional defects; our unit cell of GZO-$2 \times 2 \times 2$ contains 32 atoms that corresponds to a new $Zn_{1-x}Ga_xO$ compound with the atomic Ga-concentration of about six atomic percent ($x = 0.067$).

Ultra-soft pseudopotentials including $3d$ transition metal states in the valence band are implemented with energy cut-off of 420 eV. For reliable total energy convergence up to $N_{\mathbf{k}}$ =405 **k**-points in irreducible part of Brillouin Zone (BZ) has been used. With the chosen $N_{\mathbf{k}}$ and energy cut-off value the total energy converged within few percent. However, the density of states (DOS) convergence tests indicated that accuracy within five percent (or better) has been achieved for DOS by using at least 1270 **k**-points. This was used in present work for DOS and optics.

Optical functions of GZO are calculated within the random phase approximation (RPA) as described before [44,45]. Our calculated energy gap of 0.70 eV in bulk ZnO is substantially lower than experimental value of 3.25 eV [39]. However, it agrees well with previously reported DFT-LDA and DFT-GGA gap values [46, 47]. The widely used scissor operator correction is used in this calculation in order to account for the energy gap underestimate and enable better comparison with experimental data [45–47]. With this method, the calculated optical spectra shifted to blue.

3.4 Results and Discussion

Equilibrium LDA hexagonal lattice constants of bulk w-ZnO and doped GZO crystals are given in Table 3.2.

Substitution of Ga on Zn site (Ga_{Zn}) creates a singly occupied singlet defect state in the conduction band and thus acts as a donor in ZnO. The relaxed structure shows that in the 1^+ state, Ga-O distances are approximately 5 to 7 percent shorter than corresponding values in bulk ZnO. These values agree with those reported before for

Table 3.2.
Calculated and measured (in parenthesis) lattice parameters of bulk ZnO and GZO

	ZnO	GZO
a (Å)	3.213 (3.25[a])	3.296
c(Å)	5.185 (5.205[a])	5.294
a/c	1.614 (1.602[a])	1.607
2θ (deg)	36.65 (34.38[b])	36.50 (34.26[b])
$\Delta 2\theta$ (deg)	N/A	-0.15 (-0.12[b])

[a]Ref. [47]

[b]This work.

the local contraction in GZO [47]. However, the fully relaxed unit cell shows some increase of the lattice constants in GZO compared with ZnO (see Table 3.2). The concentration of Ga in ZnO is at the alloying level (the Ga atomic concentration is about six % in our model). Consequently, the observed increase of the lattice constant should be related to the alloying effect.

Another important observation results from the comparison between measured and calculated X-ray diffraction (XRD) spectra. The predicted XRD spectra show a shift of $\Delta 2\theta$ = -0.15 deg corresponding to the (002) reflex. This shift is comparable to the experimentally measured value of ($\Delta 2\theta$ = -0.1 deg) obtained on nano-crystalline heavy doped (up to 6 atomic percent) GZO samples fabricated in this work (see Table 3.2). We can state a good agreement between measured and calculated data. Note that our theoretical model does not account for any contributions of the structural disorder presented in nanocrystalline samples that may cause an observed disagreement between calculated and measured data. Therefore, within our approach the reported effect could be understood as a consequence of the unit cell changes that may result in structural phase transformation with further increase of Ga concentration.

3.4.1 Density of States

The calculated total densities of states (TDOS) of both bulk and Ga-doped ZnO crystals are shown in Figure 3.3. Both curves are normalized with respect to the Fermi energy.

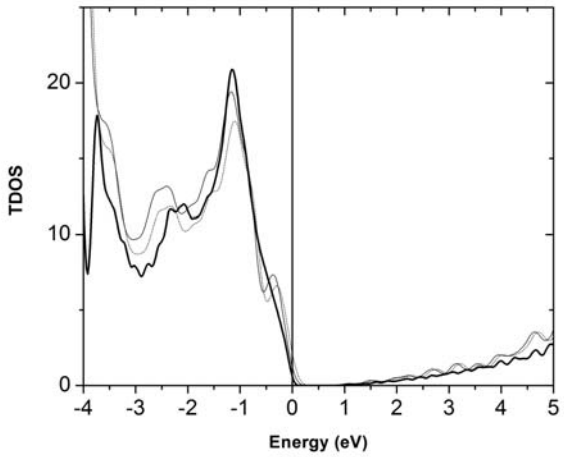

Fig. 3.3. Total Density of States of bulk (bold line) and GZO crystal of near 6 % (thin solid line) and three % Ga-concentration(thin dashed line).

The DOS spectra of the bulk ZnO show the fully occupied Zn $3d$ semicore levels which are centered at about 7 eV below the valence band maximum in good agreement with photoemission measurement data indicated a location of that maximum at $-7.4eV$ [48]. The upper valence band of ZnO has a predominant $p-$like character dominated by the O $2p$ orbitals and bottom of the conduction band is $s-$like determined by the Zn $4s-$orbitals.

Doping with Ga substantially modifies density of states, generating additional occupied defect bands at and above the top of the $v-$band (see Fig. 3.3). At such a very high doping concentration, these states are forming a new valence band maximum that will be suitable for increasing the hole concentration. Location of this maximum is Ga-concentration dependent that can be seen in Fig.3.3. However, no remarkable difference in TDOS has been noticed between 3 and 6 wt% doped GZO in agreement with the optical spectra measured at different concentration. Energy

shift and redistribution of the TDOS with increasing Ga-concentration cause the observed variations in dielectric function spectra. Based on the results of this work these changes in optical spectra are due to the re-hybridization of electronic states followed the geometry changes with increased Ga-content.

Calculated band gap values (without corrections) are $E_g = 0.70$ eV and $E_g = 0.54$ eV in undoped and Ga-doped crystals. Analysis of the total and angular resolved DOS (see Fig. 3.3) indicates that the band gap lowering (by $\Delta E_g = -0.16$ eV) is caused by the modifications (re-hybridization and re-normalization) of electronic orbitals in both valence and conduction bands, as well as structural reconstruction. Comparison between DOS data obtained with un-relaxed and relaxed unit cells indicate substantial structural reconstruction effect that we discuss before considering the XRD data (see Table 3.2 and discussion above).

3.4.2 Optical functions

It should be noted that the DFT theory version used in this work produces the Kohn-Sham eigen energy states that do not have direct interpretation as the one particle electron energy states [43]. The calculated Kohn-Sham gaps are substantially lower than measured ('gap-problem'). Consequently the quasi-particle (QP) corrections should be introduced into the theory in order to improve comparison with experiment.

In order to compare calculated optical spectra to the measured data, the QP correction in electronic structure model that compensates the substantial gap underestimate must be incorporated [43, 46, 47]. In this work we have obtained the value of the scissor-operator correction (Δ_{sci}) from a comparison with experiment.

The calculated dielectric functions are given in Fig. 3.4 (for perpendicular, o and parallel e polarizations). Our results are compared with experimental data obtained in bulk ZnO using generalized ellipsometry by Jellison and Boatner [49]. From the comparison we determined the $\Delta_{sci} = 2.55$ eV value that is used to correct the calculated spectra prior to compare with experimental results.

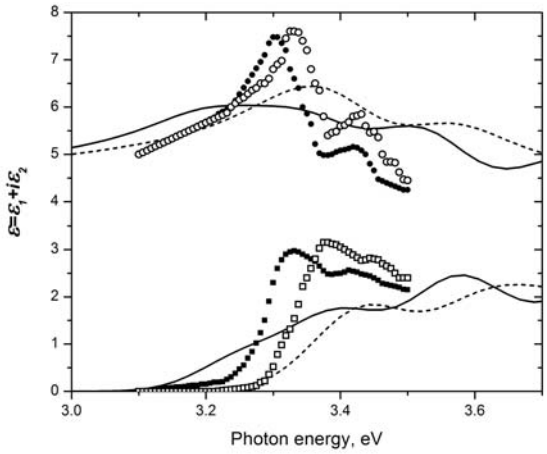

Fig. 3.4. Real (upper graphs) and imaginary (lower graphs) parts of the dielectric function spectra of w-ZnO bulk crystal calculated (lines) and measured (symbols) for ordinary (solid line, filled symbols) and extraordinary light (dashed line, opened symbols). Experimental data were obtained by generalized ellipsometry in [49].

Our value of Δ_{sci}= 2.55 eV is comparable to the 2.70 eV used by Gori et al. [46]. From the comparison between calculated and measured data on bulk ZnO we can state that our theory (DFT+Sci) correctly reproduces the measured optical anisotropy in wurtzite ZnO (see shift between ordinary and extraordinary optical constants spectra in Fig. 3.4). On the other hand, this version of the theory fails to reproduce strong peak at the absorption edge. This peak is interpreted in literature as a consequence of a strong exciton interaction [46, 50]. Inclusion of exciton effects into the band structure calculations requires numerical solution of Bethe-Salpeter equation [43,45] which is very computation-expensive and out of the scope of present work. However, as shown in this work, neglecting the exciton interaction in ZnO does not preclude us from drawing conclusions about the mechanisms that govern the optical response in doped ZnO.

Further, we consider the mechanisms that change the bandgap of ZnO upon heavy doping. The contributions of plasma excitation to the dielectric function of GZO films with 3 and 6 wt% doping in the visible and near-infrared spectral regions may be observed. The variations observed are accompanied by substantial blue-shifts in the

optical absorption edge. The following are main mechanisms that contribute to the optical response of such polycrystalline heavily doped semiconductors films [44]:

- Burstein-Moss (BM) shift
- Atomic structure distortions and reconstructions
- Alloying effect, the electron orbital re-hybridization and transformation towards new solid phase
- Exciton effects

In this paper we focus mostly on the changes in electron energy structure caused by heavy Ga-doping. The exciton contributions are neglected because it resulted in an underestimation of the absolute values of $\varepsilon = \varepsilon_1 + i\varepsilon_2$ and absence of the characteristic peak at the fundamental absorption edge.

BM-shift describes the blue-shift of the optical gap with free-carrier concentration (n) according to [39, 51]:

$$\Delta E_g = \frac{h^2}{8m^*}(\frac{3}{\pi}n)^{\frac{2}{3}}. \tag{3.3}$$

In order to understand the contribution of the doping-induced free carriers on the optical spectra in the fundamental absorption region, we calculated ΔE_g according to Eq. (3.3) and used it as an additional shift together with Δ_{sci} determined for bulk ZnO (see above). Using data given in Table 3.1 for our samples we obtained: $\Delta E_g =$ 0.38 and 0.52 eV for three and six percent Ga-doped samples, respectively. The last value gives the scissors operator equal to $\Delta_{sci} = 3.07$ eV for six percent doped GZO.

The values of Δ_{sci} obtained for doped GZO samples are used to compare the calculated $\varepsilon(\omega)$ spectra with experiment. In Fig. 3.5 the calculated dielectric functions are shown in comparison with experimental data for real and imaginary parts of $\varepsilon(\omega)$.

We state a good overall agreement between the measured data and the results of the first principles theory. Plasma contribution has been introduced into the theoretical model by adding the Drude term with parameters determined experimentally (see Table 3.1). Theoretical spectra correctly represent the shapes of the ε_1 and ε_2 curves.

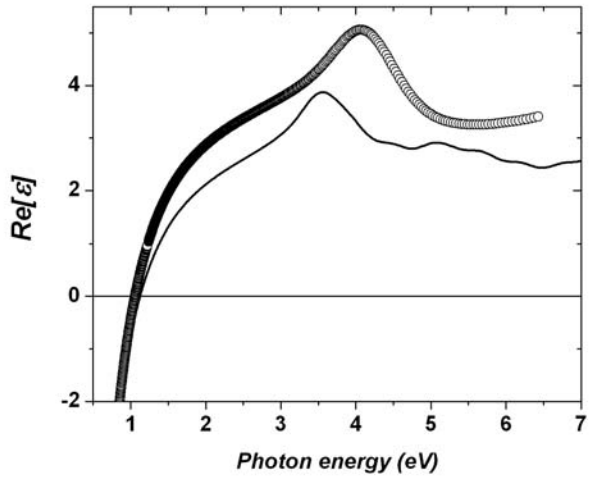

(a)

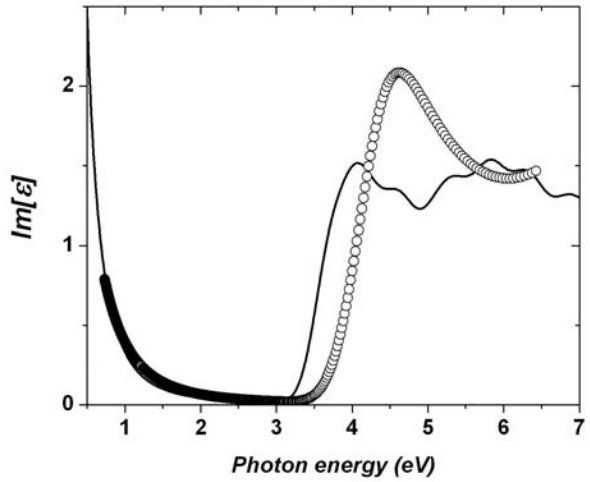

(b)

Fig. 3.5. Real (a) and imaginary (b) parts of the dielectric function spectra of GZO samples calculated (lines) and measured (symbols) for 6 wt% .

Several important issues can be extracted from a comparison between calculated and measured data. There is a substantial lowering of the measured real part values of the dielectric function as a result of Ga-doping (see Fig. 3.5). Our calculated absolute values of $Re[\varepsilon]$ are lower than experimental data. The underestimation of

dielectric permittivity values by first principles theory is due to the use of exchange and correlation method and neglecting the exciton effects described in literature [43,45,52]. The reduction of ε_1 with doping is a result of the electron energy structure modification that includes re-hybridization of electronic orbitals forming the top of the valence band and the bottom of the conduction band (see above).

Comparison between theory and experiment indicate a strong blue shift in dielectric functions spectra with increase of Ga-concentration that is substantially higher than the BM shift expected for the given Ga-concentrations. Most significant difference between theory and experiment occurs at highest studied Ga-concentration (see Fig. 3.5). The bulk values of Δ_{sci}=2.55 eV used to calculate theoretical $\varepsilon(\omega)$ spectra, are corrected on the BM shift only (0.52 eV for 6% doping). Using calculated value of E_g=0.54 eV (see above) this results in predicted energy gap of 3.61 eV which is substantially lower than the value of 3.89 eV measured here (see Fig. 3.1). Thus the measured $\varepsilon(\omega)$ spectra are remarkably blue-shifted comparing to the theory as shown in Fig. 3.5. This clearly indicates that BM effect is not the only mechanism responsible for the blue shift of $\varepsilon(\omega)$ spectra with Ga-doping.

Changes in the band structure and optical functions with the increase of the component concentration is a well-known effect in solid alloys [53]. Increase of the Ga-concentration should convert GZO into Ga_2O_3 : Zn doped oxide i.e. through the phase transition. The crystalline $\beta - Ga_2O_3$ oxide has a monoclinic crystal structure and optical gap in the ultraviolet region, near 4.7 eV [54, 55]. It is therefore expected that quasi-particle correction term, the Δ_{sci} is concentration dependent, and it will increase with the Ga-concentration. Our theory does not account any structural transformations corresponding to the phase transition. We used the super unit cell approach with the super cell symmetry corresponding to that of the host ZnO. In such a way, the orbital re-hybridization (alloying) effects are partially included in our model, and our results demonstrate that alloying effects are obviously important even at only few percent of Ga-concentration. A more advanced model should be assembled considering possible stable (or metastable) structural phases. This highlights further developments of the GZO optics theory.

In addition, we note that both our experimental and theoretical results of atomic structure study indicate a substantial increase of the inter-planar distance in the doped samples that supports structural mechanism contributing to the change in the optical functions with doping. The substantial underestimation of the calculated blue-shift of the absorption band-edge in 6 wt% GZO films as against the measured value is another factor that indicates the importance of the structural transformation effect which should be accounted by a modified theory.

3.5 Conclusion

We present the results of experimental and theoretical studies on the optical dielectric functions of gallium doped ZnO polycrystalline films that are used as a low-loss plasmonic material. The comparison of dielectric functions of heavily doped GZO films extracted from ellipsometry measurements against those calculated using first principles DFT showed that alloying effects have a significant influence on the optical properties of the films. It was shown that alloying effects are significant even at relatively low Ga concentrations of 1 wt%. This indicates that GZO that is used as a low-loss plasmonic material is not just Ga-doped ZnO, but a new alloy material altogether. It was observed that a more sophisticated model is necessary to capture these alloying effects in plasmonic GZO films. This study has provided an insight in understanding the doping mechanism of heavily doped ZnO which may be applied to other TCOs as well. Understanding the relationship between material, structural and optical properties, as well as the physical mechanism of doping and its influence on the electronic bandstructure of these materials is important for designing low-loss alternative plasmonic materials. This research direction has the potential of eventually solving the inverse design problem of designing ultimate low-loss plasmonic building blocks that can pave way for plasmonics and metamaterials towards being next-generation technologies.

4. PLASMONIC RESONANCE IN TRANSPARENT CONDUCTING OXIDES BASED NANODISK RESONATOR

4.1 Motivation

The features of LSPR have attracted great interest because of their potential applications in chemical and biological sensors [56–58], surface enhanced spectroscopy [59], integrated optical circuits [60] and nano-scale optical devices [61, 62]. The characteristic of the LSPR strongly depends on the geometry and optical properties of the constituent materials, therefore the material and the geometry should be considerately designed to achieve the required functionality.

In an aspect of materials, the recent emergence of TCOs as alternative plasmonics materials has led to the demonstration of TCO based resonant devices such as synthesized nanospheres [63–66], self-assembled standing nanorods [67, 68]. These works have shown that TCO can provide unprecedented capabilities as alternative to metal for resonant application in IR. However, the geometry of nanostructure is limited to chemical reactions. Therefore, the important step along the path to replacing conventional metals with new materials is to develop the nano-patterning techniques for realizing the novel concept of plasmonic devices. This is a very important step because most plasmonic devices are based on building blocks of nanostructured metals and dielectrics.

In this chapter, we introduce a lift-off process with electron-beam lithography (EBL), a commonly used method to pattern nanoscale devices, to produce 2D-periodic arrays of TCO nanodisks for plasmonic resonator in NIR regime. We observe localized surface plasmon resonances (LSPRs) in the TCO nanodisk array in the wavelength range from 1.6 μm to 2.1 μm. In addition, we find that the LSPR wavelength and full-width-half-maxima (FWHM) of the resonance are remarkably sensitive both to the dimensions of the nanodisks and the doping density as well

as to a subsequent thermal annealing treatment. Well-defined resonance peaks are observed, which can be dramatically tuned by varying the amount of dopant and by thermally annealing the TCO nanodisks in nitrogen gas ambient while maintaining the low-loss properties.

4.2 Fabrication Procedure (Lift-off Process)

A polarization-independent design consisting of a periodic 2D-array of nanodisks have been studied extensively with noble metal since their strong resonant interaction with light is useful in many applications such as sensors [69, 70]. In this study, I fabricated an array of 270-nm-thick GZO nanodisks with a spacing of 100 nm between adjacent nanodisks. The nanodisk diameter was varied from 250 nm to 900 nm over a number of samples. Since GZO has higher plasma frequency compared to other TCOs, GZO was mainly used in this experimental study to cover much of the NIR spectrum (including the telecommunications wavelengths).

To fabricate a 2D array of TCO nanodisks as depicted schematically in Fig. 1, a silicon substrate was first spin-coated with a 1-m-thick layer of positive electron-beam resist (ZEP 520A) at 1000rpm followed by the sample pre-bake at 180^oC for 2 min. The nanoscale pattern of cylindrical nanodisks was then exposed by EBL (Vistec VB6). The beam energy was 100 kV, and the beam current was 1.012 nA. The base dose was maintained at 320 $\mu C/cm^2$. The exposed sample was developed in ZED-N50 (n-amyl acetate) for 1 minute, and dipped in isopropyl alcohol for 30 seconds to rinse ZED-N50, and then dried in gaseous nitrogen. Prior to film deposition, a post-bake was performed at 200^oC for 30 sec. We deposited TCO films by pulsed laser deposition (PVD Products, Inc.) using a KrF excimer laser (Lambda Physik GmbH) operating at a wavelength of 248 nm for source material ablation. The TCO films are deposited with PLD system. A high oxygen partial pressure can etch the e-beam resist during the deposition process due to reaction with oxygen gas. Thus, all the films were grown with an oxygen partial pressure of 0.2mTorr (0.027 Pa) or lower. Since e-beam resist can become hard-baked from elevated substrate temperatures during a deposition process, the deposition temperature should be maintained as low

as possible in order to facilitate the subsequent lift-off process. In our studies, the substrate temperature during TCO thin film deposition was optimized at 70^{o}C.

For the lift-off process, the sample deposited with a TCO film was dipped in ZDMAC (dimethylacetamide) for 10 min and sonicated for 1 min. Most of the e-beam resist was removed during this process, but small amounts of resist remained on the edges and sides of the nanostructures. In order to remove the residual e-beam resist, the sample was dipped in PRS 2000 stripper at 70^{o}C for 30 min and then dipped in acetone for 5 min for rinsing.

4.3 Characterizations

4.3.1 Structural Characterization

The scanning electron microscope (SEM) image in Fig. 4.1(b) shows the uniformity of the nanopatterned arrays in a relatively large area of nanoscale devices. The shape of nanodisk is almost perfectly circular shown in Fig. 4.1(b). It is important to note that the deposition of the GZO layer on a patterned e-beam resist and its subsequent lift-off produces non-vertical side walls. As a result, the cross-section of the nanodisk represents a trapezoidal shape (see the inset of Fig. 4.1(a)). For morphological analysis, we scanned the sample with an atomic force microscope (Veeco Dimension 3100 AFM) to check the roughness of the nanodisk top surface. We used standard Si probe tips with the AFM in tapping mode. The resolutions of our AFM scans were not sufficient to accurately investigate the full depths of the narrow gaps between nano-disks. Hence, it is difficult to see the cross-sectional dimension of the nanodisks from the AFM image shown in Fig. 4.1(c). The root-mean-squared (RMS) roughness of the tops of the pat-terned nanodisks was about 6-8 nm. For as-deposited GZO thin films without any patterning processing, the RMS roughness is 5 7 nm. We can therefore confirm that the lift-off process does not significantly affect the surface morphology of the developed TCO material.

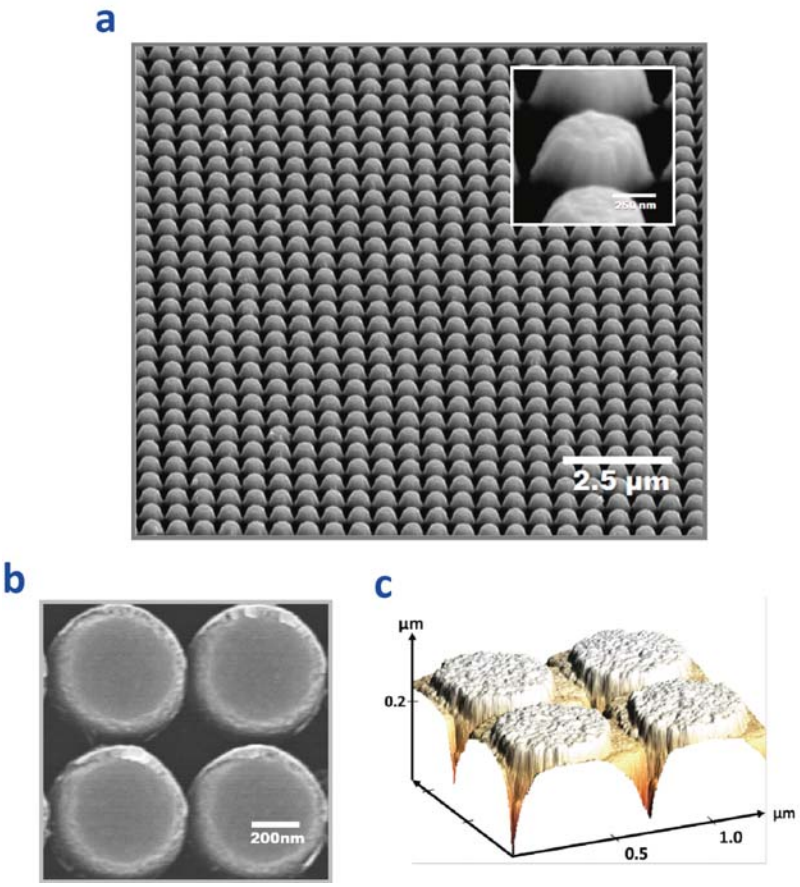

Fig. 4.1. (a) 54^o tilted SEM image of an array of GZO nanodisks with a mean diameter D=500 nm and height h=270 nm. (inset) SEM image of GZO nanodisks at high magnification. (b) Top-down view of the nanodisks showing nearly circular shapes. (c) AFM scan of the GZO nanodisks.

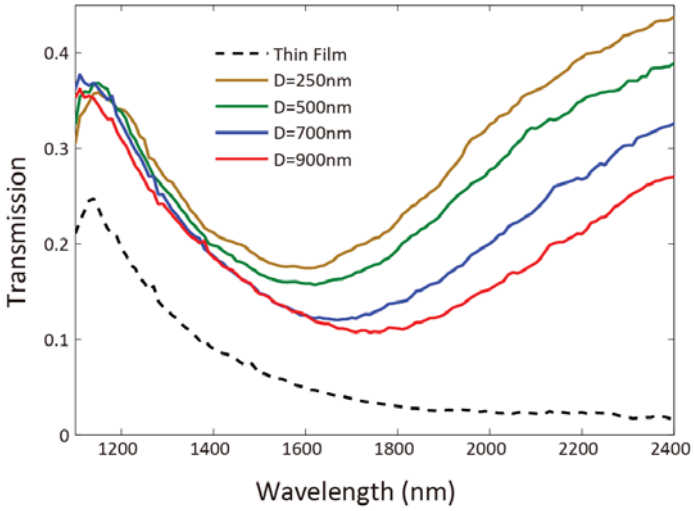

Fig. 4.2. Transmittance spectra for GZO nanodisk array samples and unpatterned GZO thin film on Si substrates with different nanodisk diameters

4.3.2 Optical Characterization

The transmission spectra of the nanodisk arrays are obtained using a V-VASE spectroscopic ellipsometer with a normally incident TE wave. The measurement is performed in the wavelength range from 1.1 μm to 2.4 μm (see Fig. 4.2). Note that absorption below 1.2 μm corresponds to phonon-assisted interband optical absorption in the silicon substrate. The LSPR wavelength and intensity depend on the size, shape, and properties of the nanostructured array. We investigate the effects of disk size and doping density on the LSPR properties.

The transmission spectra reveal well-defined LSPR peaks, and the positions of these peaks depend on both the disk size and the doping density. As the disk diameter increases (see Fig. 4.2), the resonance red shifts and becomes stronger. However, the transmission peak broadens as the disk diameter increases. This is due to the fact that the disks begin to support higher order plasmonic modes that start to overlap as the disk size increases [71, 72]. The experimental trends are verified by simulations with Finite Element Method (FEM) based commercial software, Comsol Multiphysics. Trapezoidal nanodisk structures are used with the optical properties obtained from thin films co-deposited with the nanostructures. Figure 4.3(b) shows the simulation results for the GZO nanodisks with varying doping densities. Although some minor mismatch due to fabrication imperfections exists, numerical results are in good agreement with the experiments. As discussed in previous chapter, the change of plasma frequency and optical loss depends on doping density. As the doping density of GZO increases, the films exhibit higher plasma frequency, and hence, the resonance shifts to shorter wavelengths. The optical loss of GZO is increased as reducing the doping density. The broadening of resonance peak corresponds to the increase of optical loss. In terms of the tunability of the LSPR wavelength, the peak shift arising from the change in doping density is much stronger than that caused by the nanodisk geometry.

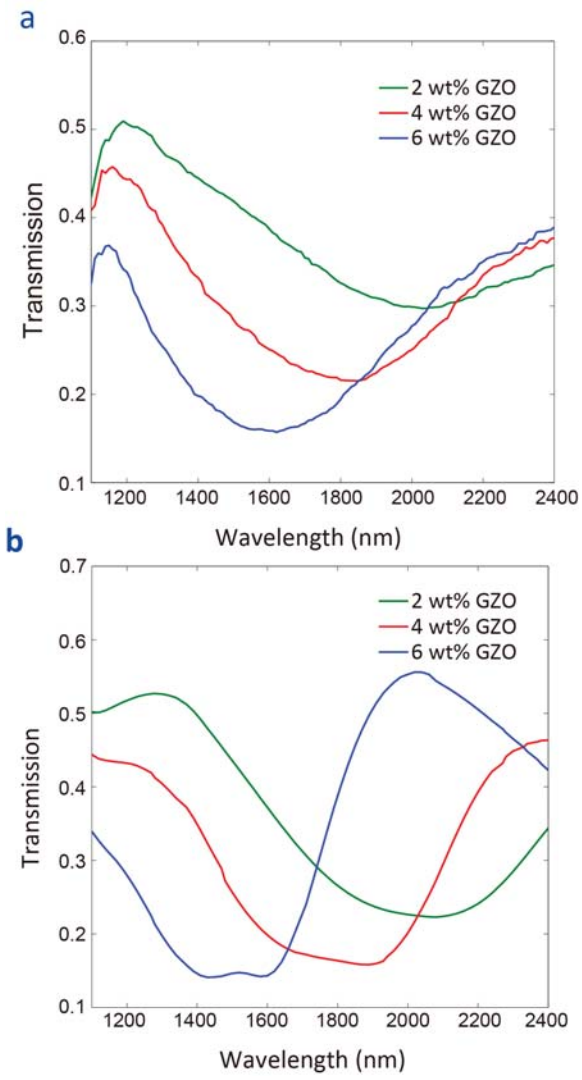

Fig. 4.3. (a) Measured transmittance spectra for the GZO nanodisk arrays (disk diameter of 500 nm) with different doping ratios in the GZO material. (b) Simulation results of transmittance spectra for GZO nanodisk arrays using different dielectric functions for films with different doping concentrations

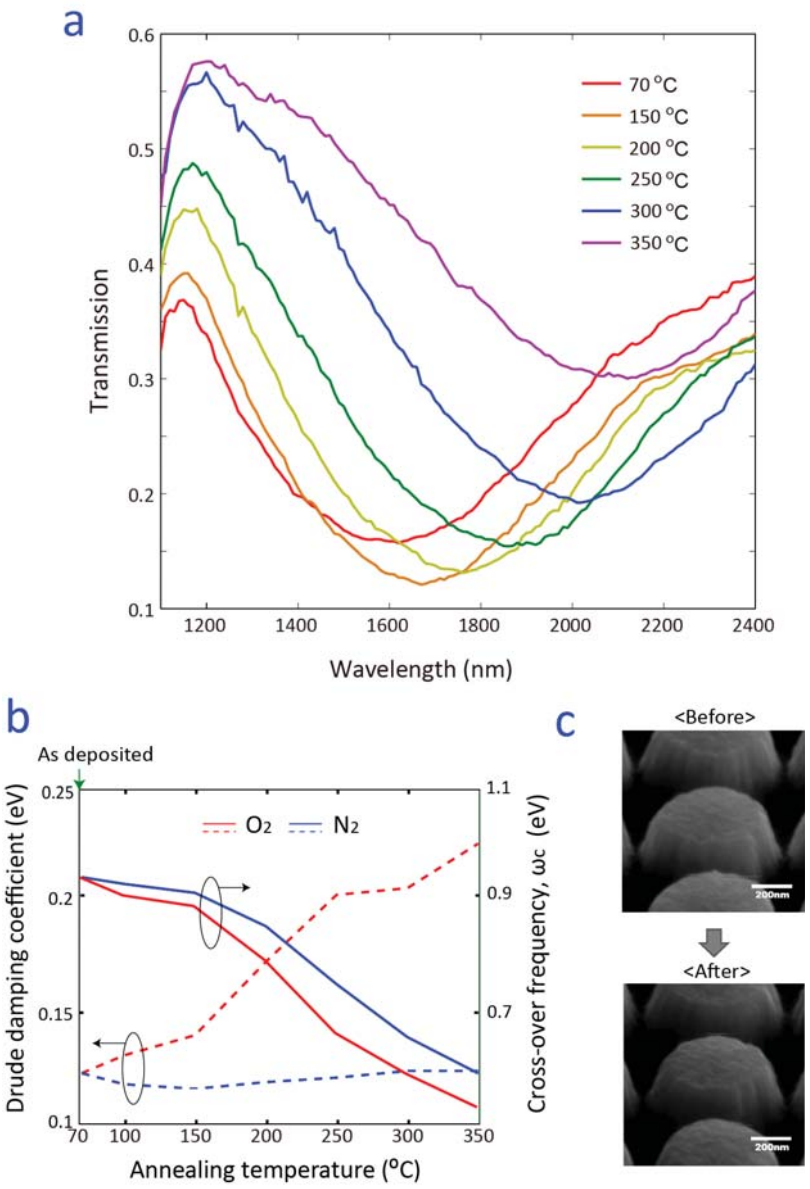

Fig. 4.4. (a) Transmittance spectra for GZO nanodisk arrays with different thermal annealing temperatures in a nitrogen ambient. (b) Drude damping coefficient and cross-over frequency (ω_c) vs. annealing temperature in either oxygen or nitrogen ambient gas. (c) SEM image of nanodisk before and after thermal treatment.

4.4 Post Annealing Process

Thermal treatments on TCO films have been well-studied in transparent electrode research in order to enhance the crystal-linity and hence, the transparency of TCO films. The effect of thermal annealing on a TCO film is strongly dependent on the temperature and the type of ambient gas. In order to characterize the effect of thermal annealing on plasmonic properties, we first investigated the annealing effect on the optical properties of TCOs with respect to two aspects: carrier concentration and optical loss. The GZO nanodisk sample was annealed up to 350^oC for an hour in nitrogen ambient to observe the effect of the annealing gas on the optical loss. The resulting transmittance spectra in Fig. 4.4(a) show that the thermal treatment can dramatically tune the LSPR peak to longer wavelengths due to reductions in the carrier concentra-tion. Post-deposition anneal offers a way to control the LSPR properties through a post-fabrication treatment without any changes in optical loss of TCOs. This allows for flexibility in the design and optimization of the LSPR nanostructure. In Fig. 4.4(b) we plot the Drude damping coefficient and cross-over frequency as functions of the annealing temperature with either a nitrogen or oxygen ambient. The Drude damping coefficient is indicative of the optical losses occurring in the material, and the cross-over frequency (ω_c) is defined as the frequency at which the real part of permittivity of the material crosses zero. Since ω_c is directly proportional to the plasma frequency (ω_p), and ω_p is proportional to the square of the carrier concentration, the plot in Fig. 4.4(b) in essence shows the carrier concentration trend with respect to the annealing temperature.

We see in the figure that the carrier concentration decreases with increasing annealing temperature for both types of ambient gas. The optical loss strongly increases after annealing in oxygen ambient, while the optical loss remains the same after annealing in the nitrogen ambient. The morphological and structural modifications incurred by the annealing treatment have already been examined in the case of noble metals. In those studies the goal was to improve quality of the LSPR properties through an annealing treatment. We carry out similar studies on TCOs in this work. The SEM image in Fig. 4.4(c) shows that there are no substantial changes in the

nanodisk shape or morphology for annealing temperatures up to 350^{o}C. Given that TCOs are ceramics, we would expect this trend to continue for higher temperatures as well. In contrast, noble metal nanostructures are known to deform when annealed at such temperatures.

4.5 Conclusion

In conclusion, we showed that standard fabrication techniques to realize nanoscale TCO-based plasmonic devices. I hope that this study can contribute to develop the fundamental skills for realization of practical devices with TCOs, especially heavily doped ZnO. From our study, we demonstrate that these materials exhibit LSPR properties similar to gold and silver nanostructures. In addition, the resonance properties strongly depend on the properties of the film such as carrier concentration, which can provide a flexibility of design of devices. Furthermore, thermal annealing in different gases altered the resonance by changing the carrier concentration in these films. At the same time, in contrast to noble metals, no significant changes in morphology, surface roughness and grain structure were observed in GZO nanodisks after annealing. The effect of the carrier concentration via annealing can be used for post-fabrication tuning of the properties of TCO devices.

5. ZINC OXIDE BASED MUTILAYERED NANODISK RESONATOR FOR BIO-SENSING IN THE INFRARED: LOCALIZED AND GAP SURFACE PLASMON

5.1 Motivation

Metal-insulator-metal (MIM) configurations have been extensively studied for negative index metamaterials (NIMs) because of their magnetic resonance and local field confinement in the insulator region, which are referred to as gap surface plasmon resonance (GSPR). As well as unconventional functionalities, it is required to study on the layered configuration of TCO in order to search the the complicate design of optical-circuit proposed by ref. [60, 73]. As reviewed in the chapter 2, TCO can be widely applicable, i.e. dielectric material in visible range and metallic or epsilon-near-zero (ENZ) material in IR range. In this work, we experimentally realize a 4 layer nanodisk resonator consisting of alternating layers of ZnO and GZO, as shown in Fig. 5.1. We study and quantify the performance of layered TCO resonator and provide guidance for designing IR plasmonic devices with highly doped oxide semiconductors for bio-sensor and wavefront engineering as well as optical waveguides. As one of the most promising applications of TCO-based MIM resonators, we demonstrate surface enhanced infrared absorption (SEIRA) used extensively in bio-spectroscopy. The strongly localized electromagnetic fields at metallic nanostructures enhance the absorption from vibrational and rotational modes of nearby bio molecules making TCO nanostructures a promising candidate for IR sensing applications. The first demonstration on the SEIRA with TCO resonator has been reported in ref. [74], however this work has studied the signal enhancement exerted by the LSPR of nanostructured ITO nanorod. In our study, we demonstrate that both LSPR and GSPR can be utilized to enhance a variation of bio-molecules for SEIRA applications.

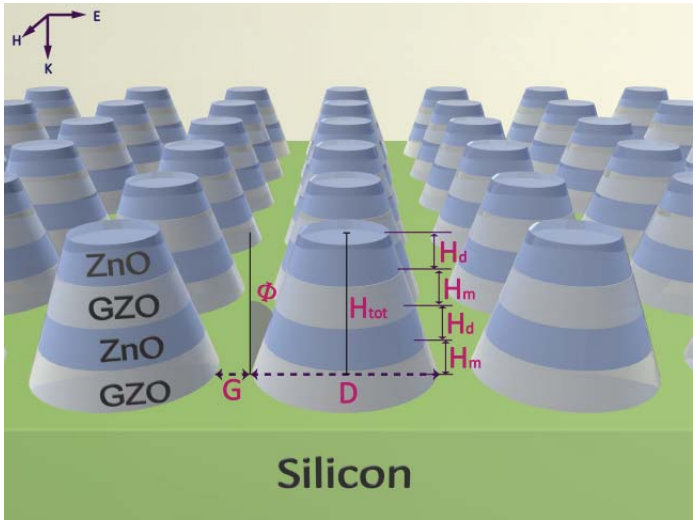

Fig. 5.1. Schematic view of an array of multilayered transparent conducting oxide nanodisk resonators and the definition of the relevant parameters. Gallium doped zinc oxide (GZO) serves as the metallic component while ZnO serves as the dielectric layer. G is the separation between adjacent nanodisks, Φ is the angle of side-wall of nanodisk, and D is the disk size. H_{tot} is the total thickness of multilayered nanodisk, and Hd and Hm are thickness of individual ZnO and GZO, respectively.

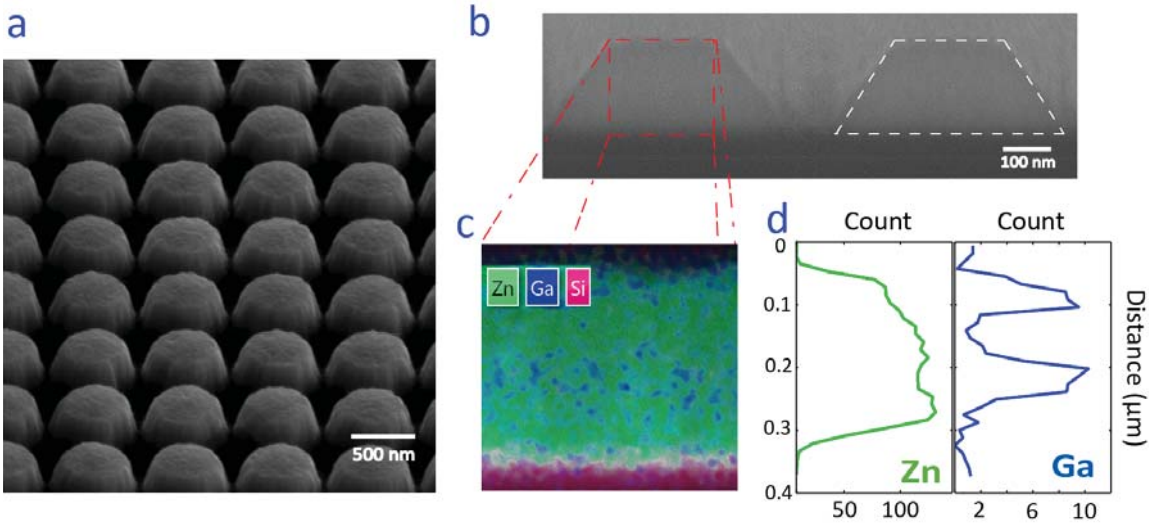

Fig. 5.2. (a) 52^o tilted SEM image of an array of GZO nanodisks with a mean diameter D= 700 nm, height H_{tot} = 320nm, and gap between two disks G= 100 nm. (b) 80^o tilted SEM cross-section image of nanodisks at high magnification. The energy dispersive X-ray spectroscopy (EDS) mapping area is marked with dashed red line. (c) EDS mapping of elements zinc, gallium and silicon of a multilayer nanodisk. (d) The line scan of Zn and Ga across the nanodisk.

5.2 Characterizations

5.2.1 Structural Characterization

By employing conventional lift-off process described in the previous chapter, we fabricate GZO and ZnO multilayer nanodisk resonators. By rotating the target in the PLD system during deposition, 4 layers consisting of alternating GZO and ZnO layers were deposited and the number of laser pulses for each target was calculated to achieve the desired thickness. The total thickness (T_{tot}) of each multilayered nanodisk is 320nm with adjacent nanodisks spaced 100nm apart in a 2-D array; furthermore, the diameter (D) is varied from 500 nm to 900 nm.

The scanning electron microscope (SEM) image in Fig. 5.2(a) shows the nanopatterned multilayer nanodisk array. It is notable that the TCO nanodisk fabricated by lift-off process produces non-vertical side walls, thus the cross-section of the nanodisk represents a trapezoidal shape (Fig. 5.2(b)). Since both GZO and ZnO are conduc-

tive, two materials cannot be distinguishable in the SEM image. To probe the multilayered configuration in nanodisk, high-angle annular dark-field imaging (HAADF) scanning transmission electron microscope (STEM) along with energy dispersive X-ray spectroscopy (EDS) was used to characterize the composition of the nanodisk. This method is highly sensitive to variations in the atomic number of atoms in the sample, therefore, it is suitable to dectect the Ga and Zinc which has atomic number of 30 and 31, respectively [75]. For EDS scanning of the cross-section of multilayer nanodisk, the nanodisk is milled with foucus inon beam (FIB) with protection layer of silicon oxide deposited with e-beam evaporator. Figure 5.2(b) shows SEM image of cross-section of milled multilayer nanodisk. EDS scanning area is marked with red square line in Fig 5.2(b). As shown in Fig. 5.2(c), three elements were mapped along the nanodisk length: zinc, silicon and gallium. EDS scan shows that gallium ion is identified throughout the sample because TEM sample was contaminated by gallium while milled by gallium ion beam with FIB. However, remarkable amount of gallium ion is detected in GZO layers and two layers of GZO are clearly observed in line scan plotted in Fig. 5.2(d). The EDS line scan along the multilayer nanodisk quantifies the doping level of gallium to the sum of zinc and gallium as 6 %.

5.2.2 Optical Characterization

In contrast with Ag or Au, one of the most important advantages of TCOs is that its intrinsic optical properties can be adjusted and tailored. The adjustability of the optical properties is achieved by altering the carrier density and electron mobility by controlling the doping rate and introducing compositional defects. Controlling the deposition parameters provides a simple method to realize nanostructures of alternating metal and dielectric layers using TCOs. ZnO is a native n-type doped semiconductor with carrier concentrations of 10^{16} cm^{-3}, thus functioning as a dielectric below wavelengths of 8 μm. However, if the carrier concentration is dramatically increased up to 10^{21} cm^{-3} with 6 wt% doping of gallium, GZO will have metal-like behavior in the NIR. Due to these properties, for operating in the IR, we can con-

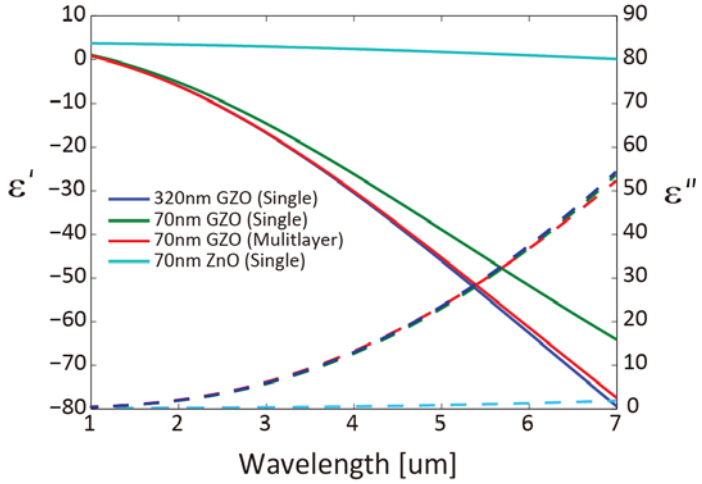

Fig. 5.3. Real (Solid line) and imaginary (dashed line) parts of the dielectric function of ZnO thin films and GZO thin films. Multilayer indicates that GZO film is sandwiched with ZnO films.

struct a multilayer configuration of nanodisks with GZO as the metallic components and ZnO as the dielectric component.

In figure 5.3, we plot the dielectric functions of ZnO and GZO thin films extracted from Drude + Lorentz oscillator parameters from 1 μm to 7 μm. It has been reported that the dielectric function of doped ZnO are dominated by Drude-Lorentz oscillator model up to around 70 μm where the additional resonance originated from the ZnO phonon resonance limits the fitting of these oscillators to retrieve dielectric function of doped ZnO [76]. As plotted in Fig. 5.3, the optical properties of GZO have a strong dependence on the thickness of the films thickness. We believe that this difference for different thickness of GZO films is caused by the interface with the substrate, which can have many carrier trap states which reduce the net carrier concentration. However, when GZO thin films are grown between ZnO layers without breaking the vacuum, the crystallinity of polycrystalline GZO thin films can be preserved because of proper lattice matching and growth orientation between GZO and ZnO. The ZnO layer helps to cure the trap states at the interface, resulting in the optical properties of the 70 nm GZO film sandwiched between ZnO to be similar to that of the 320 nm thick GZO film. Therefore, in spite of reducing the thickness of the GZO layer, we

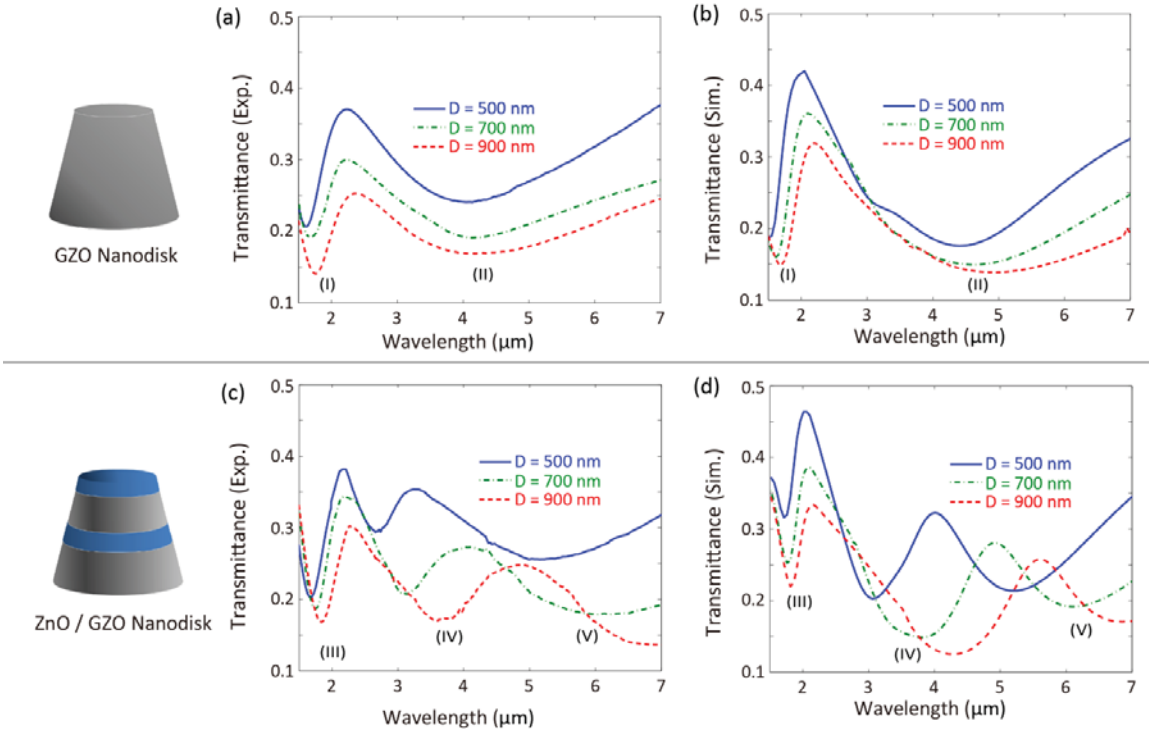

Fig. 5.4. Transmission spectra of single layer GZO nanodisk resonators ((a) experiment (b) simulation) and multilayered GZO / ZnO nanodisk resonators((c) experiment (d)simulation) with different disk size

can maintain the optical properties of the GZO films in layered geometries by using ZnO as a dielectric layer.

For comparison, we fabricated the multilayered ZnO / GZO nanodisk array consisting of 40nm thick ZnO and 120nm thick GZO (Metal:Dielectric = 1:3) and GZO nanodisks without intermediate ZnO layers (i.e. pure GZO nanodisks). The overall dimension of the single-layered GZO nanodisk array is the same as the multilayered nanodisk array. The transmission spectra were obtained using a Fourier Transform Infrared Spectroscopy (FTIR) with 0.52 numerical aperture (NA). The measurement is performed in the wavelength range from 1.5 μm to 7 μm due to the absorption from silicon substrate in visible range. Figure 5.4 shows the transmission of the GZO nanodisk array and ZnO / GZO multilayered nanodisk array. For GZO nanodisks, two strong resonances (dips) are detected at the near-infrared (NIR) and the mid-infrared

(MIR). However, multilayered nanodisks have three transmission resonances (dips) at 1.8, 3.0 and 5.2 μm wavelengths. To gain insight into the characteristic of the transmission resonances for both single-layered and multilayered nanodisk arrays, the experimental spectra are verified by simulations with Finite Element Method (FEM) based commercial software, Comsol Multiphysics. The optical properties of GZO thin film extracted from ellipsometry measurement are used for modeling of nanodisk array. In overall, the resonance dips in transmission are weaker in experiments than in simulations. This is consistent with the inevitable imperfections in nanofabrication processes which lead to surface roughness, etc. In addition, the properties of patterned TCOs change when compared to the properties of thin continuous films since nanostructuring introduces more surface area with surface traps/states that change the carrier concentration.

We first explore the resonances in a single layered nanodisk by mapping the near-field distribution at the wavelengths of 1.7 μm (I) and 4.2 μm (II), where the two strong dips are observed. At the 1.7 μm NIR dip, the electric field is localized and distributed across the top surface of the nanodisk and peaks at the corners, as shown in Fig. 5.4 (a). Considering the fact that the LSPR field decays rapidly away from the surface, the field profile at the wavelength of 1.7 μm implies a LSPR at the surface of the nanodisk. In addition, based on the Mie thoery, the scattering of spherical nanoparticle can be simply calculated by ignoring high order terms when the size of particle is smaller than the wavelength of radiation.

$$C_{ext} = \frac{24\pi^2 R^3 \varepsilon_d^{3/2}}{\lambda} \frac{\varepsilon_2}{(\varepsilon_1 + 2\varepsilon_d)^2 + \varepsilon_2^2} \tag{5.1}$$

In this equation, ε_d is the dielectric constant of the surrounding medium, ε is the complex dielectric constant of metal particle. From this equations, a resonance peak occurs whenever the condition of $\varepsilon_1 = 2\varepsilon_d$ is satisfied. Real part of permittivity of GZO at the resonance wavelength (1.7 μm) is -2.3, hence the transmission dips at 1.7 μm can be assigned as LSPR.

In contrast to the near-field distribution at resonance (I), the E-field profile at 4.2 μm shows the field enhancement on the edge at the nanodisk boundary and a weak field at the top edge of the nanodisk. As depicted in Fig. 5.4 (b), the inci-

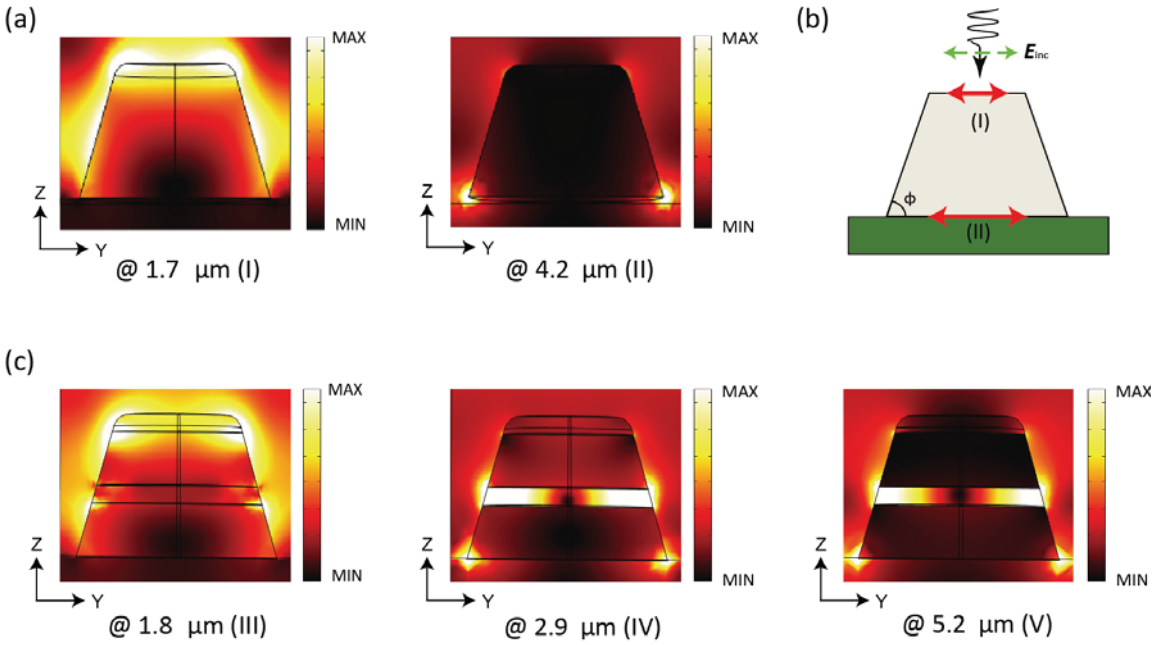

Fig. 5.5. (a) The cross-sectional and top view of near-field distribution of the GZO nanodisk (h=320 nm, d = 500 nm, g=100 nm) at the wavelengths of interests ((I) and (II) in Fig.5.4). (b) Schematic view of the interaction between nanodisk and incident light, two resonance mode can be excited due to the side-wall angle. (c) The cross-sectional and top view of the near-field distribution of the ZnO / GZO nanodisk (h=320 nm, d = 500 nm, g=100 nm, hd=40nm, hm=120nm) at the wavelength of interests ((A), (B) and (C) in Fig.5.4).

dent wave can be coupled at the two interfaces (I) and (II) (see Appendix Figure 1 for additional numerical simulation results on geometrical consideration of GZO nanodisks). Due to the large refractive index of the silicon substrate (n = 3.44) compared to air (n = 1), the EM near-field resonance of the nanodisk is broken in two, shifting a large portion of such field towards the substrate at the MIR resonance. While for NIR resonance (I), it can be noted that the EM near-field is mostly localized at the periphery of the top surface without interacting with the substrate. Qualitatively, if we consider a spherical lossless Mie scattering particle, this condition can be expressed as $2\varepsilon_{GZO} = \varepsilon_d$, where ε_{GZO} and ε_d describe the real part of the dielectric function of GZO and surrounding media, respectively. The dispersion of ε_{GZO} and the difference between the permittivity of air (ϵ_{Air}) and silicon (ε_{Si}) lead to the remarkable shift of resonance position. As the disk diameter increases, the resonance (I) is red-shifted and becomes stronger. This is due to the fact that the disks begin to support higher order plasmonic modes that start to overlap as the disk size increases [35]. Similarly, the MIR resonance wavelength (II) is also red-shifted while increasing the disk size. In fact, the resonance redshift with increasing the disk size has been observed in noble metal nanoparticles in the visible region, suggesting that the plasmonic properties and tendency of TCO-based nanostructure can be estimated by the general plasmonic properties of nanostructures with conventional metal in a different wavelength domain. Based on the understanding of the resonance characteristic of GZO nanodisks, we analyze the resonance properties of multilayered nanodisks with a similar method. Considering the field distribution of multilayered nanodisk at the wavelength of 1.8 μm as shown in Fig. 5.4 (c), the resonance in NIR (III) corresponds to the LSPR of two GZO layers separated with ZnO. This spectral feature is quite similar with the LSPR of GZO nanodisks. For the resonance (IV) at the 3.0 μm wavelength, one can see that the field is obviously enhanced inside the dielectric layer. Such high field enhancement inside the dielectric layer of MIM structure is attributed to the GSP which are propagating surface plasmon polaritons (SPPs) at the interface between metal and dielectric, observed in noble metal based MIM geometry in the visible range. Owing to the interaction of the SPPs at the two interfaces between GZO and ZnO, SPPs are slowed down and the slow-light SPP

coupled into the ZnO regime forms a standing-wave resonance under the condition of constructive interference, leading to the enhanced light-matter interaction . The resonance wavelengths (λ) have to satisfy the Febry-Perot equation as reported in the ref. [77]:

$$w\frac{2\pi}{\lambda}n_{pp} = m\pi - \varphi \tag{5.2}$$

where w is the width of the resonator, n_{pp}=$Re(\beta/k_o)$ is the real part of the mode-index of the GSP, φ is the reflection phase, and m is an integer referring to the order of the resonance [77]. The dependence of resonance wavelength on disk size is clear evidence that the identified resonance are caused by GSP. From the equation, we can notice that the resonance wavelength is linearly shifted with increasing resonator width. It is well-matched with the experimental result on variation of resonance wavelength with regards to the increase of disk size. The mismatch of magnitude of transmission spectra at 3.0 μm wavelength is ascribed to the surface roughness of side wall which can increase the scattering of light at the boundary of dielectric layer and reflected SPPs at the end of ZnO layer is reduced. Furthermore, additional intrinsic optical loss of GZO nanodisk can arise from nanopatterning of GZO layers. For the resonance at the wavelength of 5.2 μm, similar with the resonance properties of single-layer GZO nanodisk, lights gets trapped at the boundary between the nanodisk and the substrate. Notably, the multilayered GZO nanodisk sustained the two LSPRs excited in the single layered GZO nanodisk in despite of the introduction of dielectric layers.

By varying the portion of dielectric layer in multilayered nanodisk, we explore the tunability of three different types of resonances ((III), (IV), (V) in Fig. 5.4). Figure 5.6 shows the resonance frequencies in multilayered GZO/ZnO nanodisk as a function of the ratio of the dielectric layer. Since Ttot is constant (320 nm), the thickness of GZO and ZnO layers simultaneously change as the ratios are varied. For instance, 50 percent of ZnO means that the thickness of the GZO and ZnO layers are 80 nm and 80 nm, respectively. The resonances of multilayered nanodisks shift toward longer wavelength by increasing the proportion of dielectric. The variations of resonance wavelength of two LSPR ((III) and (IV)) are determined by the modified effective

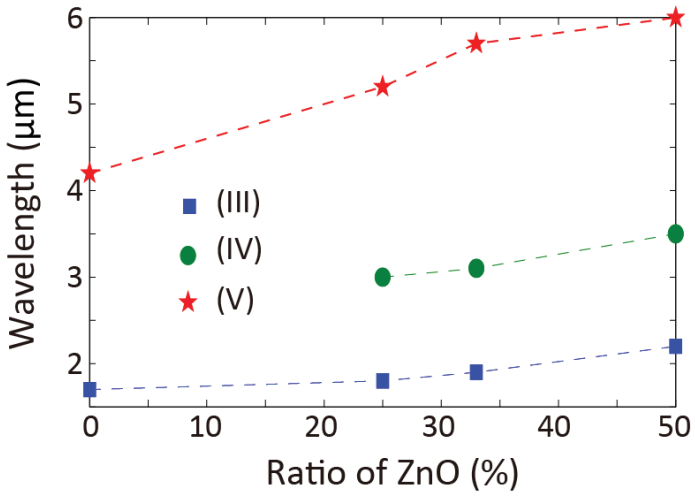

Fig. 5.6. Resonance wavelength of multilayered nanodisk resonators with different thickness ratio between ZnO and GZO as a function of percentage of ZnO.

permittivity of layered configuration. With manipulation of dielectric thickness, the effective permittivity of the nanodisk can be engineered as we desire. TCOs have small magnitude and weak dispersion of real part of permittivity compared to noble metal, therefore tunability of resonance wavelength is significant by controlling the dielectric thickness. It should be noted that the tunability of GSP resonance (II) is ascribed the change of effective index of SPP mode at the interface of metal and dielectric [78]. GSP is also easily controlled by modifying the nanostructure dimensions and/or the dielectric layer thickness. Building a multilayered geometry is the efficient and feasible approach to engineering the resonance properties of plasmonic nanostructures without changing the properties of the materials.

5.3 Surface Enhanced Infrared Absorption (SEIRA)

We characterize the capability of multilayered nanodisk arrays for mid-infrared SEIRA. For the characterization of SEIRA of GZO / ZnO nanodisk resonator, the layered nanodisk with the ratio of 1 to 3 between ZnO and GZO is covered with an octadecanethiol (C18H37SH) layer. The dominant absorption from vibrational modes of octadecanethiol (ODT) molecules are located very close to the GSP resonance of the multilayered nanodisk [79]. To cover the nanodisk with an ODT layer, the sample was exposed to 1 mM solution of ODT in ethanol during 24 hours; the samples were then taken out of the ODT solution, thoroughly rinsed with ethanol to remove any excess amount of unbound ODT molecules, and dried with Nitrogen gas. SEM images in the Fig. 5.7 (a) shows the formation of ODT layers on top of nanodisks [80]. The ODT layer is randomly aggregated during solvent evaporation, but the thickness of the layer is, on average, around 20nm and the coverage over the entire array is 70%.

IR spectra were obtained with FTIR spectrometer and normalized with transmission of multilayer nanodisk without ODT layer as shown in Fig. 5.7 (b). The reference spectrum also was taken from a bare silicon substrate. From the measurements, distinguishable absorption peaks of ODT molecules assigned from CH stretching vibrations are as follows: symmetric CH2 stretch (2848 cm^{-1}), symmetric CH3 stretch (2871 cm^{-1}), antisymmetric CH2 stretch (2915 cm^{-1}), and antisymmet-

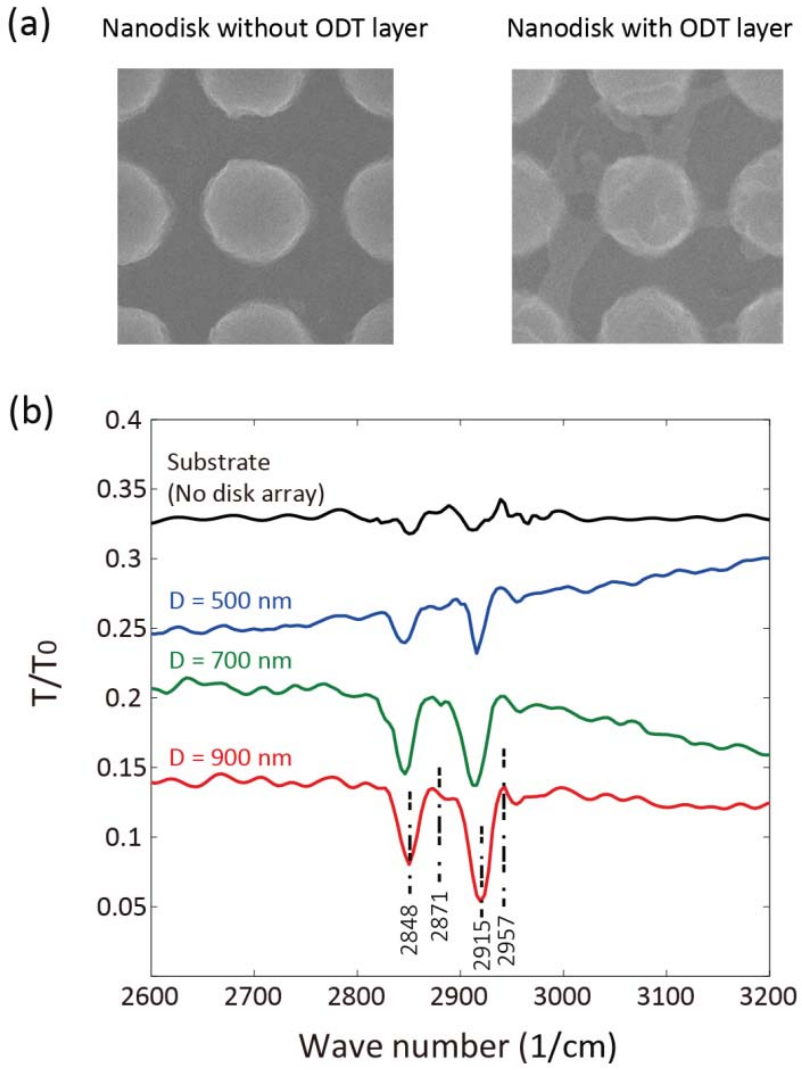

Fig. 5.7. (a) SEM images of multilayered nanodisk array without (left) and with octadecanethiol layer (right). (b) SEIRA transmission spectrum T/T0 of ODT on multilayer nanodisk array with the 1:3 ratios between ZnO and GZO.

ric CH3 stretch (2957 cm^{-1}) [79]. Even though the aggregated ODT layer makes it difficult to directly compare between spectrum from bare silicon substrate and from multilayer nanodisk, it is noted that the absorption spectrum of ODT molecules become stronger as the GSP resonances are well-aligned with the ODT absorption spectral lines. For example, we are able to clearly detect the very weak ODT absorptions (2871 cm^{-1} and 2957 cm^{-1}) from multilayered nanodisk with 900nm diameter nanodisks whose GSP resonance exists at 2700 cm^{-1} (3.7 μm). Therefore, GSP resonances on metallic oxide semiconductor based nanostructure can have the ability to observe very weak molecular absorption at their resonance and have been able to resolve the presence of nanoscale species.

5.4 Conclusion

We have introduced that the plasmonic behavior of a plasmonic structure can be manipulated by creating multilayer nanostructure consisting with subwavlength thickness of metal and dielctric layer. Experimental result demostrates that the multilayer nanodisk shows the shift of plasmonic resonance by varying the thickness ratio. Similar with layered nanostructure with noble metals, GSPR are excited in the MIR range due to strong field confinement in dielectric layer. Compared with single-layer resonator, the remarkable tunability is ascribed by increasing the dielectric layer. Additionally, We investigated the performance of GZO/ZnO multilayer nanostructures for SEIRA spectroscopy. We believe that multilayer TCO configurations could pave the way for engineering the optical properties of practical resonant plasmonic device in the IR range and for realizing TCO-based IR devices for bio-sensing and spectroscopy.

6. TRANSPARENT CONDUCTING OXIDES BASED METASURFACE FOR CONTROLLING THE POLARIZATION STATE OF LIGHT

6.1 Motivation

Flat photonics is an emerging field in nano-optics that utilizes the concept of metasurfaces [11, 81]. With the advent of metasurfaces, fabrication challenges associated with volumetric metamaterials can be easily overcome. Metasurfaces can push conventional optical components to the subwavelength scale, paving the way for ultra-compact devices and on-chip optical processing. By altering the phase of the incoming light, metasurfaces have enabled unique applications, such as 3D holograms [82, 83], flat lenses [12, 84, 85], beam splitters [86, 87] and waveplates [88, 89] with a device thickness of only a fraction of the wavelength. Significant attention has been paid to create and detect circular polarization at the nanoscale for advanced optical signaling and sensors [90,91]. With noble metals, metasurfaces, which consist of arrays of orthogonally coupled nanoantennas [92,93] and V-shaped antennas [88], have been used to demonstrate wave plate operation with deeply subwavelength profiles. Although these plasmonic metasurfaces have achieved the desired function, they pose integration challenges, exhibit considerable optical losses in transmission mode, and do not offer switchability/tunability of their optical properties. For practical applications, it is more desirable to fabricate these metasurfaces with a versatile, tunable, and CMOS-compatible material. In this work, we experimentally realize a TCO metasurface to control the polarization of light in the reflection mode, spanning a broad bandwidth in the NIR regime. The metasurface is realized interleaving two orthogonal patterned nanorod arrays made of GZO. A similar design has been proposed and experimentally demonstrated with silver (Ag) as the plasmonic component to operate in the visible range [93]. To achieve the quarter-wave plate functionality, in this design the two perpendicular nanorods resonate at approximately equal

amplitudes and a phase difference of $\pi/2$ in orthogonal polarizations. Compared to noble metals, TCOs have a relatively less dispersive dielectric function, which offers a broader bandwidth of operation for TCO-based metasurfaces in the NIR range. Additionally, through a post annealing process, we can control the carrier density in TCO, thus further tuning the efficiency and bandwidth of the realized metasurfaces. This method describes in the previous chapter. Furthermore, we show that changing the angle of incidence our TCO metasurfaces can provide QWP functionality in two distinct NIR optical-bands. To the best of our knowledge, this is the first demonstration of TCO-based metasurfaces controlling the phase of an incoming wave and achieving QWP functionality in the NIR range.

6.2 Design of QWP Metasurface

Two orthogonal nanorods provide the array element for our metasurface as shown in Fig. 1a. Each nanorod acts as a local antenna when excited at the resonance by the incident light with a particular direction, amplitude, and phase. Since the phase of the scattered fields sharply varies with the frequency around the nanorod resonance, it is possible to tailor the phase shift between the scattered waves of two orthogonal nanorods by slightly changing their relative lengths. In our design, we chose the lengths of orthogonal nanorod pairs such that linearly polarized light incident on our metasurface at an angle θ is converted to circularly polarized light over a particular spectral range. As illustrated in Fig. 6.1 (b), the polarization angle ϕ is defined in the plane of the metasurface. To ensure a broad bandwidth, the horizontal rods are joined into a continuous strip and vertical rods are reduced to squares as shown in Fig.6.2.

We obtained the optimized dimension of each GZO rod through an analytical model provided in the recent work on metasurfaces based on orthogonally aligned silver nanorods. The analytical model ensures that the reflection matrix of such metasurface can be described as

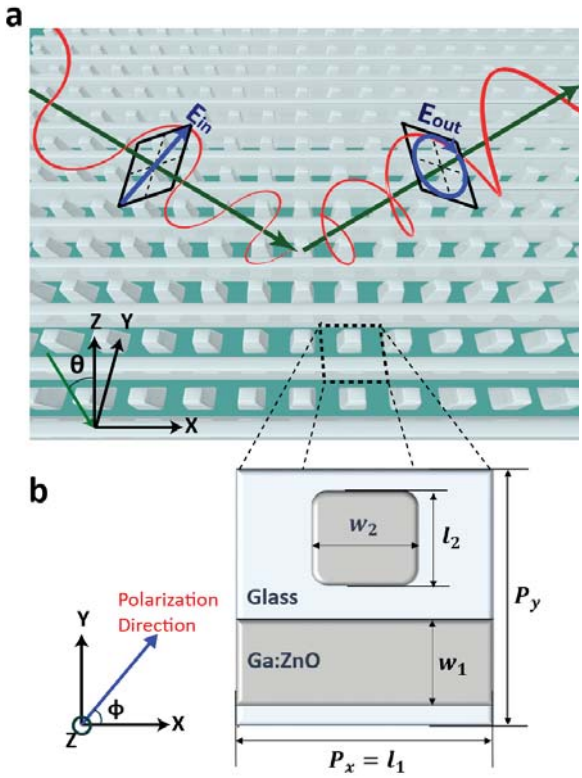

Fig. 6.1. (a) Schematic view of an array of metal oxide nanostructures forming a metasurface. θ is the angle of incidence. The metasurface serves as a quarter wave plate by converting a linearly polarized light to circularly polarized light in reflection mode. (b) Unit cells of plasmonic metasurfaces and the corresponding geometrical parameters. ϕ is the direction of polarization of incident wave. l_m and w_m (m = 1, 2) are the length and width of two nanorods, respectively. P_x and P_y is the periodicity in x and y directions. P_y is fixed at 750 nm, but P_x is varied from 550 nm to 750 nm to change the coupling efficiency of the two orthogonal nanorods.

$$R = \begin{bmatrix} R_{xx} & 0 \\ 0 & R_{yy} \end{bmatrix} = \begin{bmatrix} -\frac{j\mu_0\phi fc\cos\theta}{p_x p_y}\frac{a_{xx}}{1-C_{int,xx}a_{xx}} & 0 \\ 0 & -\frac{j\mu_0\phi fc\cos\theta}{p_x p_y}\frac{a_{yy}}{1-C_{int,yy}a_{yy}} \quad 0 \end{bmatrix}$$

(6.1)

where f is the frequency of operation, c is the speed of light in vacuum, μ_0 is the permeability of free space, and C_{int} is the interaction dyadic. From the three-axial ellipsoid quasi-static polarizability with semiaxes w/2, l/2, and t/2, the polarizability tensor (a_{ii}, i=x,y,z) can be calculated as $a_{ii} = \phi/2 * wlt(\varepsilon_{GZO} - \varepsilon_m)/[3\varepsilon_m + L_i(\varepsilon_{GZO} - \varepsilon_m)]$, where L_i is the shape factor and ε_m is the permittivity of the surrounding medium of the nanorod. Considering the fabrication limitations, we optimize the metasurface with a constant thickness (t = 550 nm), width (w_1 = 250 nm and w_2 = 300 nm), and length of the horizontal nanorod (l_2 = 300 nm), but vary the length of horizontal nanorod (l_2) from 550 nm to 750 nm with 100 nm increment to control the bandwidth of operation. As the length of the vertical nanorod is varied, the periodicity in the x-direction is also varied accordingly. TCO-based QWP metasurfaces require that the thickness (t = 550 nm) of the nanorods is one order of magnitude larger than a corresponding silver metasurface due to its low magnitude of real part of permittivity.

6.3 Fabrication Procedure (Dry-Etching Process)

To fabricate the metasurface, we developed a dry-etching technique with bilayer resists Hydrogen Silsesquioxane (HSQ) for the masking layer and PMMA for the sacrificial layer. As shown in the schematic of the fabrication flow (Fig. 6.2 (a)), a 550-nm-thick GZO film is deposited on a glass substrate by pulsed laser deposition (PVD Products, Inc.). On top of the deposited GZO film, we spin-coat a 100 nm-thick layer of PMMA at 4000 rpm followed by the sample pre-bake at 80^oC for 5 min. Once the PMMA layer is baked, we spin-coat a 500-nm-thick layer of HSQ. The sample is pre-baked again at 80^oC for 5 min. The nanoscale pattern of QWP is then exposed

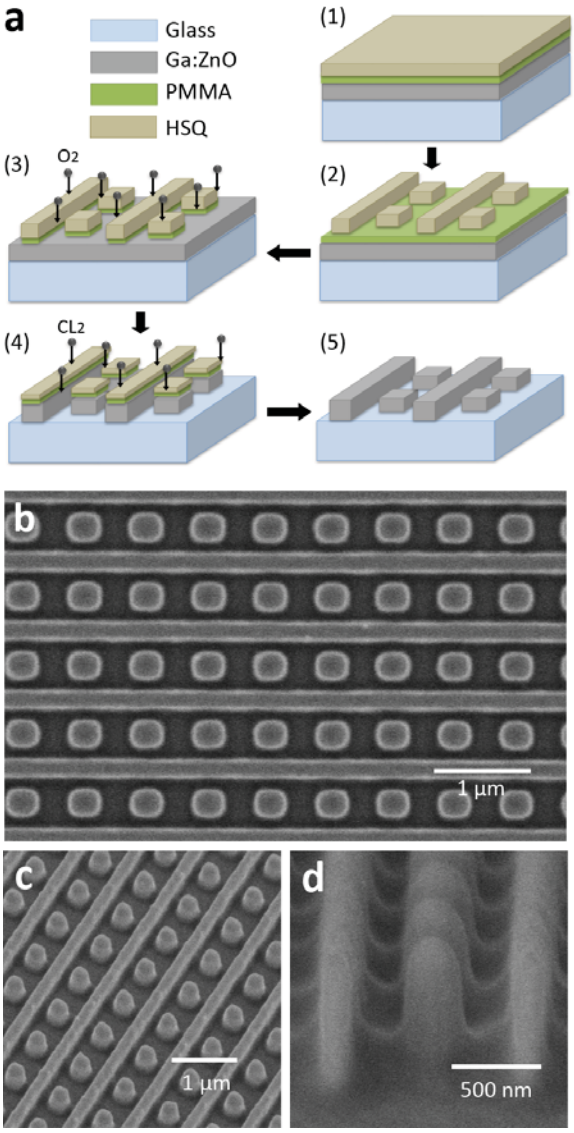

Fig. 6.2. (a) Process flow for fabrication of GZO metasurfaces using ion reactive etching with bilayer resist. 1) Spin-coating of PMMA and HSQ layer over GZO film, 2) E-beam lithography of HSQ resist. 3) O_2 RIE etch of PMMA with HSQ as the etch mask, 4) CL_2 RIE etch of GZO with HSQ and PMMA as the etch mask and 5) Removal of PMMA and HSQ etch mask with Acetone (b) Top view, (c) 30^o tilted view and (d) cross-sectional (75^o tilted) view of FE SEM image of fabricated GZO metasurface.

by EBL (Vistec VB6). An exposed sample is developed in Tetramethylammonium hydroxide (TMAH) 25% for 1 minute, and dipped in DI water for 30 seconds to rinse off the TMAH, and then dried in gaseous nitrogen. The PMMA layer is etched by oxygen gas and the TCO film is etched by chlorine gas with reactive ion etching (RIE). GZO film is etched down 1.2 times faster than HSQ, hence 500 nm-thick nanorod can be patterned with 500 nm thick HSQ as the masking layer. When the design of the QWP metasurface is transferred to the GZO layer, the sample is dipped into Acetone to remove the PMMA layer with the remaining HSQ. The field emission scanning electron microscope (FE SEM) images in Fig. 6.2 (b-c) provide a different view of the fabricated GZO metasurface. The shape of the square particles becomes rounded during the etching process, but the size of structures is maintained as the original design.

6.4 Optical Characterization

The corresponding reflection spectra for the orthogonal linear polarizations (R_{xx} and R_{yy}) along the two rods with different periodicity in the y-direction are presented in Fig. 6.3 (a). We notice that R_{xx} and R_{yy} have two pronounced resonant dips in the reflection spectra. To gain insight into the characteristics of the reflection resonances for both R_{xx} and R_{yy}, we validate the experimental spectra with numerical simulations using a commercially available software based on the Finite Element Method (COMSOL Multiphysics), as shown in Fig. 6.3 (b). We extracted the optical properties of GZO by performing variable angle spectroscopic ellipsometry (VASE) measurements (V-VASE, J. A. Woollam) on GZO thin films; the extracted values are then used as the material properties in our simulation. The metasurface is simulated as a single unit cell with periodic boundary conditions.

GZO thin films are metallic for the wavelengths longer than 1.18 μm. Overall, the resonance dips are weaker in the experiments than in the simulations due to inevitable fabrication imperfections such as the rounded shape and roughness of the sidewall. In addition, the optical properties of patterned TCOs change when compared to the properties of thin continuous films, because nano-fabrications introduce surface

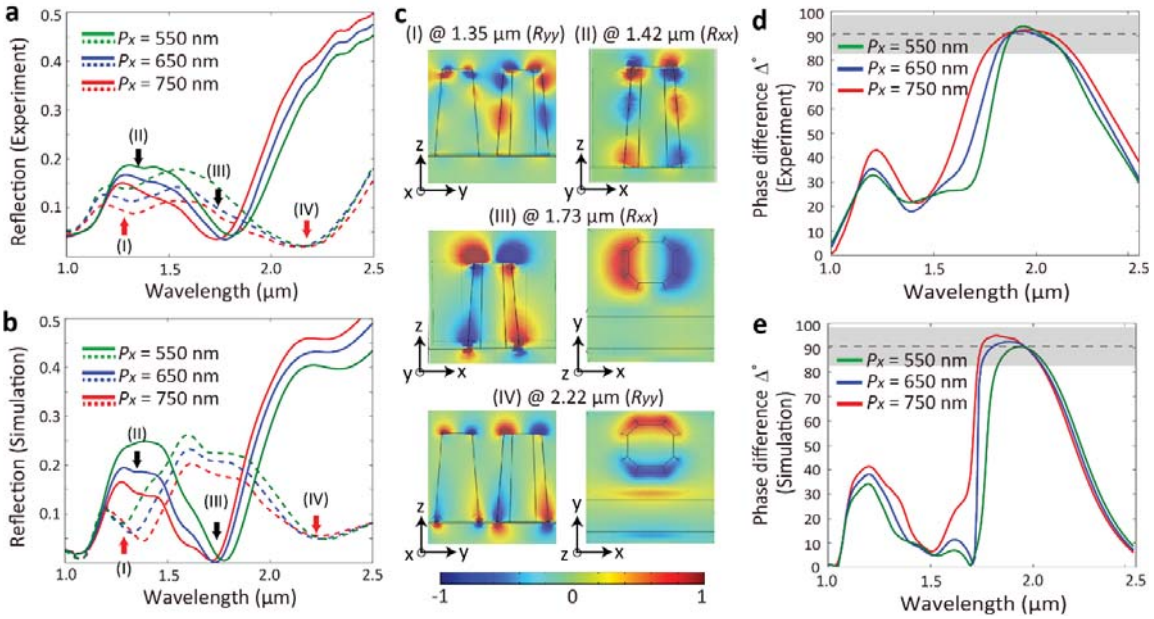

Fig. 6.3. (a) Experiment and (b) simulation of reflection spectra of GZO metasurfaces for orthogonal linear polarizations: R_{xx} (solid line) and R_{yy} (dashed line). (c) Cross-sectional, top-view near-field distributions of GZO metasurface ($P_y = 750$ nm) at the wavelengths of interests ((I), (II), (III) and (IV) in reflection spectrum (a) and (b). The intensity of electric field is normalized. (d) Experimental and (e) simulated phase difference Δ of reflected light between two orthogonal polarizations (x and y) for 18^o oblique incident light. The periodicity of unit cell in y-direction is varied from 550 nm to 750 nm. The incident light is polarized to 45^o with respect to x-axis.

traps/states that change the carrier concentration. We first explore the resonances dips in y-polarization by mapping the near-field distribution at the wavelengths of 1.35 μm (shown in Fig. 6.3 (c) (I)) and 2.22 μm (Fig. 6.3 (c) (IV)), where the strong dips are observed. The cross-sectional map of the electrical fields z-component (E_z) at the resonance in Fig. 6.3 (c) (I) shows that the fields are mostly enhanced between the nanorod and particles. Considering the permittivity of GZO and the periodic arrangement of the metasurface, we can assume that the metasurface acts as a periodic geometrical grating, therefore the absorption is enhanced at the resonance shown in Figure 6.3 (c) (I). This feature is quite similar to the strong absorption of ITO nanorod arrays, which were attributed to the guided modes of surface plasmon of periodic arrays of nanostructures. The field profile at the wavelength of 2.22 μm implies a localized surface plasmon resonance (LSPR) of the square particle in the direction of y-polarization. Two resonances in R_{yy} labelled with (II) and (III) at 1.42 μm and 1.73 μm also support different modes of resonances, as shown in near field distributions in Fig. 6.3 (c). To verify the performance of our metasurface, we measured the phase difference between two orthogonal polarizations of the reflected light using spectroscopic ellipsometry. In general, spectroscopic ellipsometry measurement collects the difference of the phase (Δ) and the amplitude (ψ) between two orthogonal polarization states. As described in Eq. 6.2, we can extract Δ of two orthogonal polarizations (x and y component) from the ellipsometry measurement

$$\varphi = \frac{R_p}{R_s} = \tan(\psi) e^{i\Delta} \tag{6.2}$$

where R_x and R_y are the reflection of x and y polarization states and ψ is the ellipsometry parameter. Figure 6.3 (d) shows the measured Δ of our metasurface at an angle of incidence = 18^o. In the wavelength range highlighted by the grey area in the plot, the Δ between two orthogonal polarizations is $90^o \pm 9^o$ (with 10 % margin), ensuring that the metasurface functions as a QWP in this spectral range. As expected from our numerical simulations, the TCO metasurface provides a wide range of quarter-wave plate functionality; for the case where P_x = 750 nm, the bandwidth is around 450 nm from λ = 1.75 μm to λ = 2.2 μm. The QWP bandwidth is reduced when the length (l_1) of the horizontal rod is decreased; this is due to the

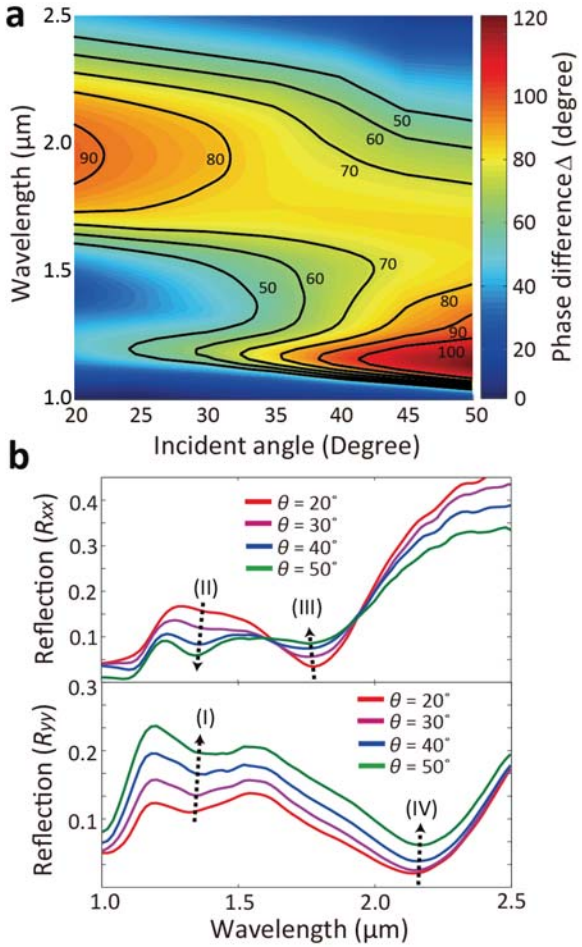

Fig. 6.4. (a) Experimental phase difference Δ of GZO metasurface as a function of angle of incidence in the spectral range between 1 μm and 2 μm wavelength. The incident light is polarized to 45^o with respect to x-axis. Solid lines show corresponding phase differences with respect to different wavelengths and angles of incidence. (b) Reflection in x and y polarization (R_{xx} and R_{yy}) at various angles of incidence.

shift of the dipole resonance in R_{xx}. Our ellipsometry results match well with our numerical simulations on the bandwidth variation with regards to the periodicity. Some discrepancies with the simulations may arise, partially due to the scattered light from fabrication defects such as sidewall roughness.

Consistent with the spectral range between two resonances corresponding to the excitation of the LSPR in two orthogonal polarizations, it is interesting to observe the phase variation between resonance (I) and (II) associated with the non-localized surface plasmon. By properly adjusting the size of each nanorod for detuning res-

onances, we are able to realize a 90^o phase difference between the two resonances. Another method to control the phase difference is to change the angle of incident light. As presented in Fig. 6.4 (a), the spectral range is varied by changing the incidence angle. With increasing angle of incidence, the phase difference between the two LSPR resonances (III) and (IV) is reduced, whereas the phase difference between the resonance (I) and (II) is increased. At an oblique angle of incidence, incoming light with polarization $= 45^o$ can be decomposed into x and y components, respectively transverse-magnetic (TM) and (TE) waves, respectively. For the TE case (R_{yy}), as the incidence angle increases gradually, a slight red shift of the reflection dip can be observed, with an increased reflectance over the entire visible region. In contrast to the behavior of the TE mode, the TM case (R_{xx}) drives a blue shift of the two resonances (I) and (IV); additionally, we see a strong absorption of the resonance associated with the non-localized plasmon mode (I) for the increasing angles of incidence. Due to the opposite direction of resonance shifts with different polarizations, the two resonances (I) and (II) are getting closer so that the phase difference eventually reaches to $\Delta = 90^o$ at the angle of incidence $\theta = 35^o$, whereas the phase difference between the two resonances (III) and (IV) are getting smaller due to the increment of separation. Therefore, the TCO metasurface can span two spectral ranges in the NIR by controlling the incident angle. However, it only covers a very narrow range of wavelengths between resonances (I) and (II).

To demonstrate our metasurface functionality as a waveplate, we measure the degree of circular polarization at $\lambda = 1.9$ μm and 2 μm by rotating a linear polarizer in front of a detector and measuring the reflected power, as depicted in Fig. 6.5 (a). We generated the infrared light using an amplified Ti:sapphire femtosecond laser followed by an optical parametric amplifier which was tuned over the 1.6-2 μm spectral range. We chose P_x=750 nm, which provides the broadest bandwidth. A 45^o polarized plane wave ($\phi = 45^o$) illuminated to the metasurface, the same angle of polarization of the reflected light from the bare glass. The angle of incidence is fixed to 18^o to be consistent with the ellipsometry measurement. In comparison to the phase difference at the wavelength of 1.6 μm where the metasurfaces cannot serve as a QWP, a high degree of circular polarization close to unity can be maintained at the

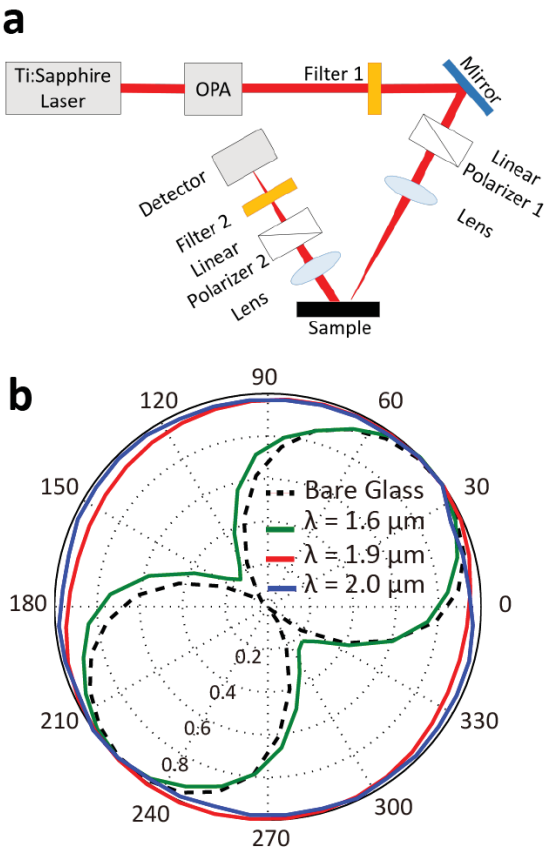

Fig. 6.5. (a) Schematic of the optical set-up to characterize the degree of circular polarization. Laser light is generated using an amplified Ti:sapphire femtosecond laser in combination with an optical parametric amplifier for infrared generation. Filters 1 and 2 are infrared longpass and bandpass filters, respectively; filter 2s central wavelength was selected at 1.6, 1.9, and 2.0 μm depending on the wavelength of operation. Linear polarizer 1 defines the polarization of incoming wave ($\phi = 45^o$), and linear polarizer 2 is rotated while collecting the reflected power from the metasurface. (b) State-of-polarization analysis for the reflected beam at = 1.6, 1.9, and 2.0 μm. The reflected beam from a bare glass is collected at =1.9 μm.

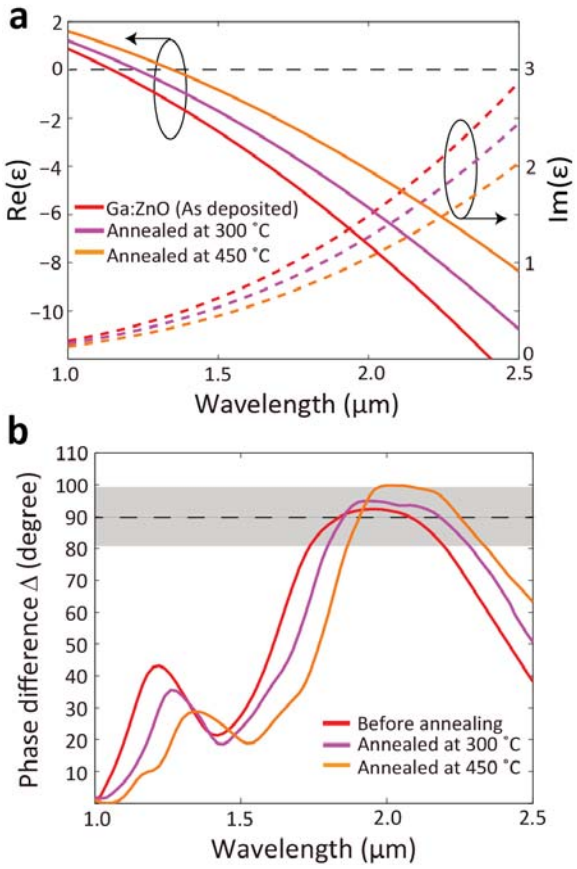

Fig. 6.6. (a) Dielectric functions of GZO thin film. GZO films are annealed at 300^oC and 450^oC. (b) Phase difference Δ of reflected light from metasurface before and after annealing. Angle of incidence is 18^o and the incident light is polarized to 45^o with respect to x-axis. The periodicity of unit cell in y-direction is 750 nm.

wavelength of 1.9 μm and 2 μm. These results substantially confirm the waveplate functionality of our GZO metasurface, and demonstrate that our devices are able to achieve a high degree of circular polarization (98%) in the reflection mode over a broad range in NIR.

One efficient method to engineer the resonance frequency of metal oxide based resonators without changing the design of the metasurface is post-growth annealing. As shown in Eq. 6.1, the polarizability tensor is a function of the permittivity of the metallic component. Thus the operational range of the GZO metasurface can be readily tuned through post-growth annealing. Figure 6.6 (a) presents the optical properties of GZO films annealed at different temperatures in the nitrogen

gas ambient for one hour. These results show the tunability of optical properties of GZO through the annealing process. As a result of the decrease of intrinsic carrier density, we observe the shift of cross-over wavelength with an increasing annealing temperature. This variation can be directly utilized to tune the functionality of GZO based QWP metasurface as shown in Fig. 6.6 (b). We note that the operational range of the waveplate is shifted as much as the crossover wavelength of GZO thin film is shifted by the post annealing process.

6.5 Conclusion

We have experimentally demonstrated a plasmonic metasurface in the NIR using highly doped metal oxides that operates as a quarter-waveplate in the reflection mode. The broad bandwidth of QWP functionality is achieved due to slow dispersion of the dielectric function of GZO. The experimental results agree well with our theoretical predictions and numerical simulations. Our TCO metasurface can be flexibly applied for a variety of spectral ranges by simply controlling the angle of incidence or adjusting its intrinsic properties through a post annealing process or other (electrical or optical) means, unprecedented with noble metal based metasurfaces. In addition, conventional nanofabrication techniques are employed to realize TCO metasurfaces that offer easy integration with other nanophotonic devices that may require special polarization states. We believe that the broadband performance, versatility, compactness as well as integration advantages of the demonstrated waveplate pave the way to many practical applications of TCO metasurfaces in optical and nanophotonic technologies.

7. TRANSPAERENT CONDUCTING OXIDES AS ENZ SUBSTRATE OVER THE PLASMONIC ANTENNA

The radiation pattern and the resonant wavelength of nanoantenna are significantly influenced by the interaction between the nanoantenna and the substrate on which it lies. The role of dielectric or metallic substrate upon this response has been studied intensively so far; however, limited investigations have been undertaken for substrates exhibiting epsilon near zero (ENZ), which offer novel light-matter interactions. Novel interactions are predicted from substrates exhibiting ENZ, which offer high impedance to electromagnetic waves and uniform phase distributions within its domain and therefore, the radiation from the resonating antenna is preferentially directed away from the substrate surface. Thus, the resonance of the antenna gets pinned at the frequency where the real permittivity transitions at the ENZ point. In this study, we demonstrate this pinning of the Au antenna resonance at the ENZ point, demonstrating the generality of this phenomenon with Au nanoantennas resonant in both the near-infrared on TCO-based ENZ substrates usch as AZO and GZO for the former spectral range (ENZ points at =1.29 μm and 1.19 μm respectively). The directionality of the electromagnetic radiation from the nanoantennas on ENZ and dielectric substrates were compared using both experiments and electromagnetic simulations.

7.1 TCOs as ENZ materials

ENZ is unique properties on materials exhibiting negative real-permittivity, therefore resulting the wavelength where the real-oermittivity becomes zero. Such ENZ regime has led to a wealth of predicted novel light-matter interactions [94]. In practice, the ENZ response is observed near the plasma frequency of plasmonic materials or the longitudinal optic phonon frequency of polar dielectrics. The ENZ material provides three predominant impacts upon the local electromagnetic fields. First, ENZ

materials exhibit an exceptionally high impedance with the surrounding environment. This in turn will limit the penetration of incident fields into the ENZ material under most conditions, preferentially redirecting it back towards its source. However, under certain circumstances, incident fields can penetrate through an ENZ medium, exhibiting the phenomenon of supercoupling. Secondly, the wavelength within an ENZ material will become exceptionally large, approaching infinity. This in turn implies that minimal phase variation of the electromagnetic fields is observed over the course of many free-space wavelengths [95, 96]. Finally, as the index of refraction is directly proportional to the permittivity at optical frequencies, for low-loss materials with small imaginary part of permittivity at the ENZ condition, n also becomes vanishingly small.

An exciting phenomenon is derived from materials with very low values of permittivity, eventually becoming zero value [60, 97, 98]. So far, artificial ENZ material have been realized in the microwave and alternating layers of Ag and SiN with subwavelength layer thicknesses have been demonstrated as ENZ materials since their permittivity tensor elements can achieve values near zero in the visible spectral range [94, 99, 100]. In contrast to man-made ENZ materials, the permittivity of TCOs can effectively go to zero at NIR regime due to the Drude dispersion of permittivity, therefore they are already available in nature [16, 101]. By utilizing TCOs as ENZ materials, we can simply overcome the difficulties of manufacturing ENZ materials for higher frequencies. Even though noble metals shows ENZ properties in the visible and ultraviolet range, these materials has relatively high loss which can degrade the performance of ENZ devices. However, TCOs exhibit a small imaginary part of permittivity at their respective ENZ points and thus provide the low-loss media necessary for exploring the ENZ phenomena. In addition, we can have huge flexibility on a design of ENZ materials with with the position of this ENZ point tunable by changes in the carrier concentration.

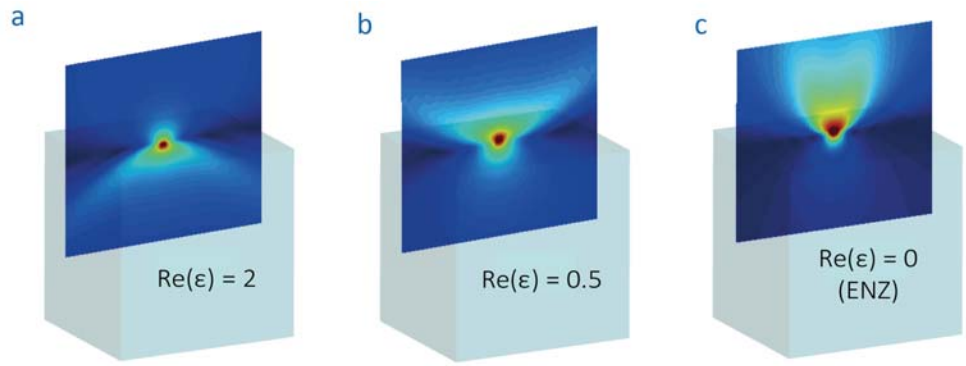

Fig. 7.1. Schematic view of radiation of nanoantenna lying on the substrate with real part of permittivity of (a) Re(ε)= 2, (b) Re(ε) = 0.5, and Re(ε) = 0

7.2 Theoretical Study

When an antenna is located on an interface between two dielectric media, e.g., the air-dielectric interface, most of the radiation is directed into the medium with higher relative permittivity, exhibiting a radiation pattern with the main beams directed at an angle related to $sin^{-1}(n_1 n_2)$ where n_1 and n_2 are the refractive indices of two media with $n_1 > n_2$ [102], and the angle is measured from the normal to the interface. Fig 7.1 (a) sketches an example of such a radiation pattern, emanating from a infinitely long, two-dimensional (2D) wire antenna placed on the interface between air and a semi-infinite (loss-less) dielectric medium with dielectric constant $Re(\epsilon) = 2$. In this example, the radiation pattern, which is primarily propagating into the dielectric region, has two main beams directed at 45 and -45 degrees off normal. This feature has been exploited in applications such as subsurface radar imaging and sending. However, when an antenna is placed on top of low-permittivity substrates, the air above is the medium with higher relative permittivity and therefore the antenna radiation will be predominantly directed into the air, which is a denser medium. This is demonstrated in Fig. 7.1 (b), where we show the radiation pattern of the same 2D wire antenna, but here the loss-less substrate is assumed to have the dielectric constant of 0.5. We notice that the pattern still has two main beams, however they are now pointing into the air, albeit again directed at angles 45 and -45 degrees off normal. This behavior is modified significantly when the substrate is an

ENZ material, as shown in Fig. 7.1 (c). Here we present the corresponding radiation pattern for the wire antenna on a loss-less ENZ material, whereby the resultant beam pointed towards the zenith. Similar features have been discussed theoretically for layered structures, however, experimental verification of these predictions have thus far been lacking. In what follows, we will discuss our experimental results whereby these novel nanophotonic phenomenon are experimentally realized in the NIR spectral regimes.

For any substrate, radiation of the nanoantenna will be distributed over two parallel paths, one through the substrate and the other through the superstrate, which in this case is air, with the relative efficiencies of these paths defined by the dielectric function of the substrate [103–105]. The resonant frequency of such nanoantenna arrays has been derived for such systems and can be described as Eq. 7.1:

$$\lambda_{res} = 2n_{eff}(L_{eff} + 2\delta), \;\; n_{eff} = \sqrt{\varepsilon_{eff}} = \sqrt{\varepsilon_{sub} + \varepsilon_{air}} \tag{7.1}$$

where L_{eff} is the effective length of antenna and δ is the extension of field at the tip of antenna. Assuming the local medium around the antenna is air, effective permittivity of the surrounding medium of atenna can be described as Eq. 7.1. As the real part of permittivity of substrate approach zero, n_{eff} also becomes vanishingly small. This in turn implies that L_{eff} becomes exceptionally large. Therefore, as the antenna length is increased, the resonant frequency will shift toward ENZ wavelength, and eventually will be pinned at the wavelength where ε_{eff} is zero.

7.3 Experiment

Periodic arrays of 40 nm tall and 50nm wide, Au nanorod arrays of varying lengths were fabricated on either a 1.4 μm thick AZO or GZO film deposited on a glass substrate. For comparison purposes, Au nanorods were also fabricated on top of undoped zinc oxide (ZnO), which acts as a purely dielectric substrate in the NIR. As shown in Fig. 7.2 (a) and (b), the antennas were tilted at 45 degrees in reference to the array periodicity so that polarization-selective measurements could be employed to probe the in- and out-of-plane components of the nanorod radiation pattern. The

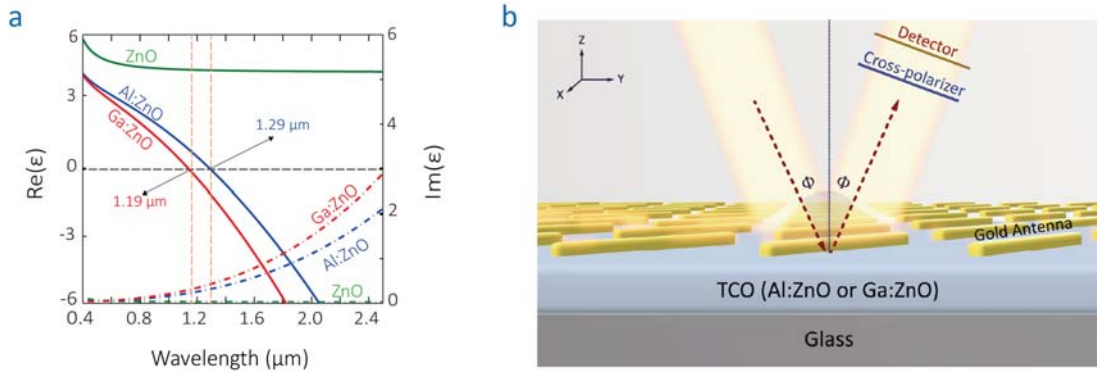

Fig. 7.2. (a) Real (solid lines) and imaginary (dashed lines) parts of the dielectric function of TCO films - Ga:ZnO, red lines, and Al:ZnO, blue lines. The ENZ points are at 1.19 μm and 1.29 μm for Ga:ZnO and Al:ZnO respectively. Real and imaginary part of the undoped ZnO dielectric function is also shown with green lines. (b) 45^o-tilted nanorod is sitting on a TCO layer deposited on a glass substrate. The incident light is directed at the antenna at an angle of incidence of $\Phi = 20^o$, and the cross-polarized reflection is detected.

incident light was directed at the sample surface at 20^o angle of incidence (Φ), and the reflection spectra was collected in the cross-polarized configuration (Fig 7.2 (b)). The resonant excitation of surface plasmons within the nanorod result in a scattering of light with electric field components aligned along both the x- and y-axes. Therefore, by only radiation from the antenna with an electric field component along the x-axis is measured.

To demonstrate the pinning of antenna resonance at the ENZ point, we fabricated nanorod arrays with fixed periodicity of 700 nm. The length of nanorods was varied from 300 to 800 nm. Note, that as the antennas are rotated 45^o with respect to the principal axes of the array periodicity, the length of the rods can exceed the periodicity (Fig. 7.3(b)). The corresponding cross-polarized resonance spectra are shown in Fig. 7.3(c) for Au antennas of 400, 600, and 800 nm lengths on Al:ZnO, Ga:ZnO and ZnO with a fixed periodicity of 700 nm. Similar to prior work using plasmonic nanorods on dielectric substrates, the resonant frequency of the Au nanorods on the undoped ZnO film exhibit a large spectral red-shift with increasing nanorod length. In contrast, the antenna resonances exhibit a drastically reduced red-shift on the Al:ZnO and Ga:ZnO substrates, appearing to become pinned at the ENZ condition

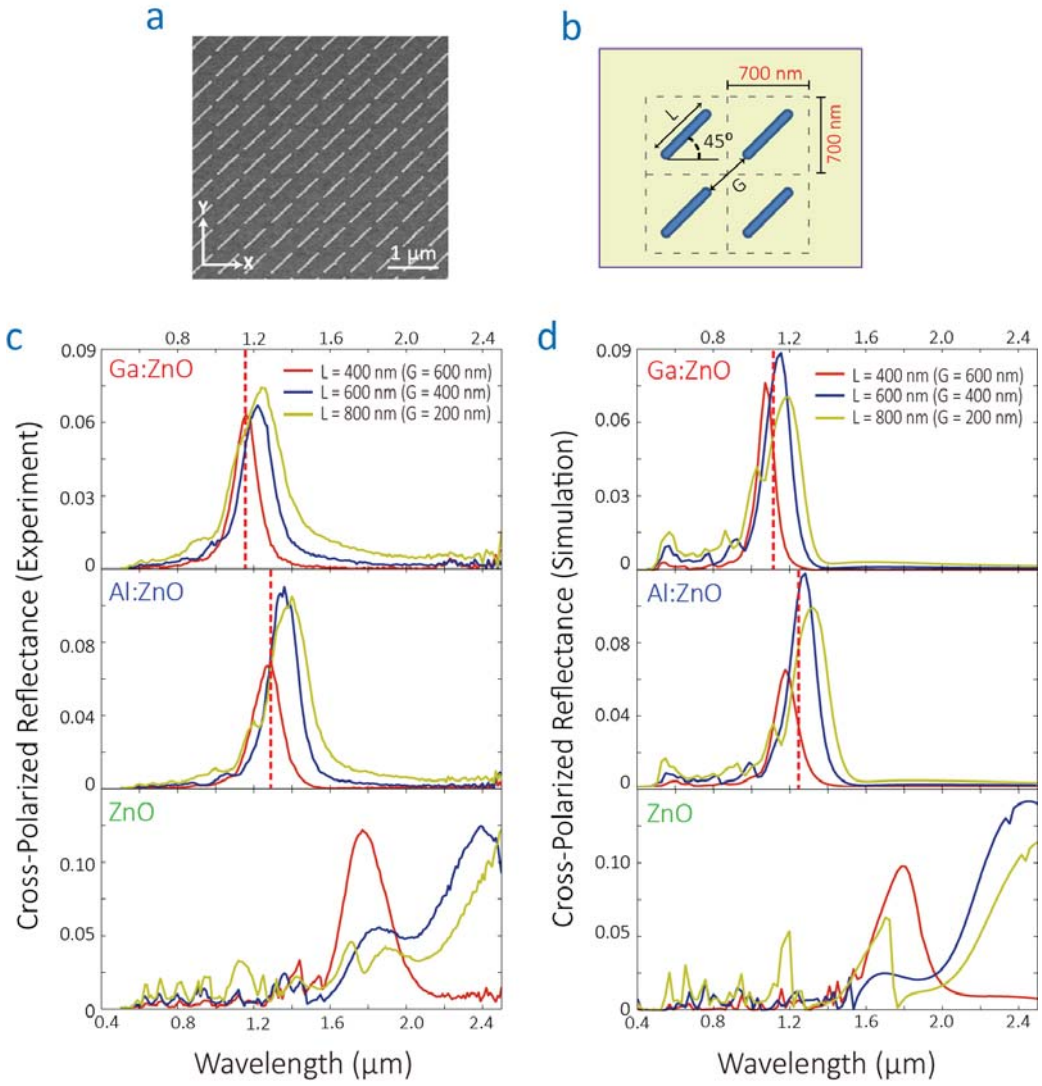

Fig. 7.3. (a) SEM image of Au nanorod array on TCO layer. Well-aligned 45^o-tilted nanorods are uniformly fabricated. (b) The dimension of nanorod array. The period of nanorod array is fixed at 700nm. Experiment (c) and simulation (d) data of cross-polarized reflection spectra of nanorod array, deposited on TCOs (Ga:ZnO and Al:ZnO) and dielectric (ZnO). Vertical Red dashed line indicates the ENZ points for Al:ZnO and Ga:ZnO.

(dashed vertical line in Fig. 7.3 (c)). This minimal spectral shift is observed despite a doubling of the antenna length. As shown in Fig. 7.3 (d), finite element method (FEM) simulation (Fig. 7.3 (c) right) is in good agreement with experimental results.

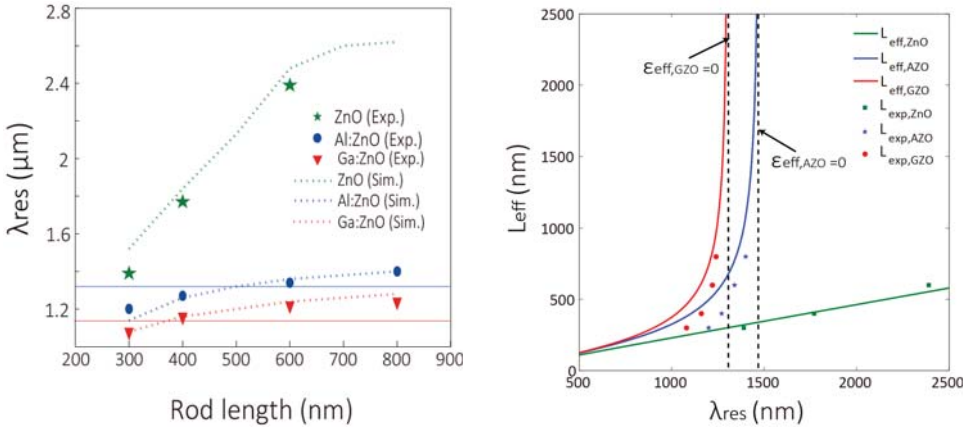

Fig. 7.4. (a) Resonance wavelength of nanorod antenna array sitting on Ga:ZnO, Al:ZnO and ZnO as a function of rod length comparison of numerical simulations (Sim.) vs. optical characterization (Exp.) (b) Effective length of antenna as a function of resonance wavelength. The experimental (real) length of antenna is plotted at the resonance wavelength of respective antenna length.

For direct comparison, the resonant frequencies as function of nanorod length are provided in Fig. 7.4 (a) and it is clear that the pinning effect, whereby the resonance frequency asymptotically approaches a ENZ frequency of the substrate, albeit over a limited range of nanorod antenna lengths. However, as discussed below, results using SiC as the ENZ substrate clearly depict the pinning effect over a broad range of nanoantenna sizes. As discussed in theory section, the effective antenna length will become extensively large at the ENZ point. As shown in Fig. 7.4 (b), the resonance wavelength of antenna is approaching the wavelength where the effetive permittivity is zero, the effetive length becomes large, and in turn the resonance of antenna is pinned at the wavelength where the effective permittivity of surrounding medium is zero.

As demonstrated in Fig. 7.1 (a), on a conventional dielectric substrate, the resonant antenna radiation will be preferentially forward-scattered into the substrate due to its higher refractive index in comparison to the ambient. On the other hand, as Re(ε) of the substrate becomes lower than the ambient, the radiation is instead preferentially back-scattered (Fig. 7.1(b)). To explore the resultant radiation patterns from the Au antennas within the dielectric and ENZ spectral regimes of the

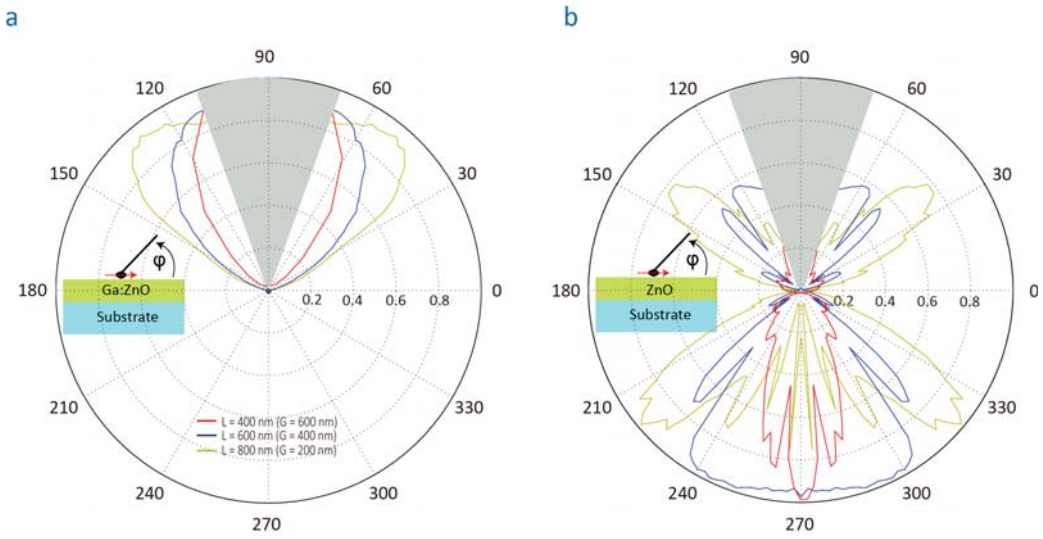

Fig. 7.5. (a) Radiation pattern of nanorod antenna with three different lengths (400, 600 and 800nm) on Ga:ZnO substrate at ENZ wavelength (1.19 μm). (b) Radiation pattern of nanorod antenna with three different lengths on ZnO substrate at ENZ wavelength (1.19 μm).

substrates, the far-field dipole radiation pattern of Au antenna on TCOs was measured using ellipsometery. As shown in Fig. 7.5 (a) and (b), the radiation of antenna on Ga:ZnO is almost 100% back-scattered into the ambient (air) at ENZ wavelength, regardless to varying the length of antenna. However, the radiation in the presence of a dielectric substrate ZnO is emitted over a large solid angle, with primary beams directed at 45 degree and -45 degree off normal, similar with simulation result in Fig. 7.5 (a). From this measurement, we ensure that the ENZ layer can therefore isolate the dipole (nanorod in this experiment) and tailor the radiation pattern according to its optical properties. Furthermore, the corresponding reduction in $n_s ub$ results in the wavelength within the ENZ material approaching infinity, thus negligible variations in the phase of the electromagnetic fields will be observed, even over distances in excess of several free-space wavelengths.

7.4 Discucssion

We have demonstrated that drastic modifications to both the resonant frequency and radiation direction of emitted radiation from local dipole emitters occur in the presence of an ENZ substrate. While the case of the dielectric substrate are consistent with prior results in the literature, the nanorods on an ENZ substrate were shown to exhibit a pinning of the resonant frequency at the ENZ condition, independent of the resonator length. Furthermore, this was coupled with a modification in the radiation pattern, whereby the emission was confined to a very small solid angle centered about the zenith. Such an effect can be useful for overcoming the geometric dispersion of emitters used in sensors, isolating various plasmonic devices for on-chip nanophotonic devices, in flat optics designs and in beam steering applications. These applications are possible because of the availability of low-loss plasmonic and polar dielectric materials which behave as bulk ENZ materials within the IR spectral range.

8. CONCLUSION AND FUTURE OUTLOOK

In the preceding chapters, we have shown the evaluation of TCOs as metallic building block in plasmonic and MMs system for IR application, and various type of plasmonic devices with TCOs - nanodisk plasmonic resonator, multilayered TCO resonator for bio-sensor and QWP TCO metasurface as well as the potential capability of TCOs as ENZ medium in the range. At the beginning of this study, only a few of literature was available because it was new approach to develop the field of nanophotonics. For the last decade, there was remarkable progress in the research on alternative plasmonic materials including TCOs. I hope our work contributes to the some of these advances and demonstrates that TCO is an excellent platform for practical approach to realize the plasmonic devices. Tunable optical properties and the compatibility of TCOs as successful alternatives to noble metals can provide huge flexibility to design of devices. In addition, newly emerging concepts such as ENZ can be explored with these low-loss materials. The research in this direction is fairly open-ended, and provides an excellent opportunity to explore and develop new functionalities. The development of materials, both for plasmonic and dielectric materials, will be essential for the further advances in plasmonics.

Lastly, I would like to suggest some of direction to further to further explore the plasmonic devices based on TCOs:

- The minimum optical loss (ε")of TCOs at ENZ wavelength is roughly 0.3. Even though this value is lower than optical loss of metals at their ENZ wavelength, the optical loss limit the impact of ENZ phenomenon. Further optimization or development of post-processing for relaxation of optical loss of TCOs can improve the efficiency of ENZ device.

- There are two possible approach to design the dynamic device with TCOs; one is optical pumping and the other is electrical-biasing. So far some of work on dynamically tunable device with ITO has been reported. However, doped ZnO

based tunable device is not demonstrated yet. Experimental demonstration of the electrical or optical tunable device with doped ZnO will be interesting topic.

- Tunneling effect and Ferrell-Berreman Modes of ENZ materials can lead to some potentially novel hybrid devices.

REFERENCES

REFERENCES

[1] D. R. Smith, J. B. Pendry, and M. C. K. Wiltshire, "Metamaterials and negative refractive index," *Sci.*, vol. 305, no. 5685, pp. 788–792, 2004.

[2] J. B. Pendry, D. Schurig, and D. R. Smith, "Controlling electromagnetic fields," *Sci.*, vol. 312, no. 5781, pp. 1780–1782, 2006.

[3] H. A. Atwater, "The promise of plasmonics," *Sci. American*, vol. 296, no. 4, pp. 56–62, 2007.

[4] W. Cai and V. M. Shalaev, *Optical metamaterials: fundamentals and applications*. Springer Verlag, 2009.

[5] L. Novotny and B. Hecht, *Principles of nano-optics*. Cambridge university press, 2012.

[6] W. L. Barnes, A. Dereux, and T. W. Ebbesen, "Surface plasmon subwavelength optics," *Nature*, vol. 424, no. 6950, pp. 824–830, 2003.

[7] M. L. Brongersma and V. M. Shalaev, "The case for plasmonics," *Sci.*, vol. 328, no. 5977, pp. 440–441, 2010.

[8] S. Lal, S. Link, and N. J. Halas, "Nano-optics from sensing to waveguiding," *Nat. Photon.*, vol. 1, no. 11, pp. 641–648, 2007.

[9] A. Poddubny, I. Iorsh, P. Belov, and Y. Kivshar, "Hyperbolic metamaterials," *Nature Photonics*, vol. 7, no. 12, pp. 948–957, 2013.

[10] Z. Jacob, L. V. Alekseyev, and E. Narimanov, "Optical hyperlens: far-field imaging beyond the diffraction limit," *Optics express*, vol. 14, no. 18, pp. 8247–8256, 2006.

[11] X. Ni, N. K. Emani, A. V. Kildishev, A. Boltasseva, and V. M. Shalaev, "Broadband light bending with plasmonic nanoantennas," *Science*, vol. 335, no. 6067, pp. 427–427, 2012.

[12] A. Pors, M. G. Nielsen, R. L. Eriksen, and S. I. Bozhevolnyi, "Broadband focusing flat mirrors based on plasmonic gradient metasurfaces," *Nano letters*, vol. 13, no. 2, pp. 829–834, 2013.

[13] R. F. Oulton, V. J. Sorger, D. Genov, D. Pile, and X. Zhang, "A hybrid plasmonic waveguide for subwavelength confinement and long-range propagation," *Nature Photonics*, vol. 2, no. 8, pp. 496–500, 2008.

[14] J. A. Dionne, K. Diest, L. A. Sweatlock, and H. A. Atwater, "Plasmostor: a metal- oxide- si field effect plasmonic modulator," *Nano Letters*, vol. 9, no. 2, pp. 897–902, 2009.

[15] P. R. West, S. Ishii, G. V. Naik, N. K. Emani, V. M. Shalaev, and A. Boltasseva, "Searching for better plasmonic materials," *Laser Photon. Rev.*, vol. 4, no. 6, pp. 795–808, 2010.

[16] G. V. Naik, V. M. Shalaev, and A. Boltasseva, "Alternative plasmonic materials: beyond gold and silver," *Advanced Materials*, vol. 25, no. 24, pp. 3264–3294, 2013.

[17] D. A. Bobb, G. Zhu, M. Mayy, A. V. Gavrilenko, P. Mead, V. I. Gavrilenko, and M. A. Noginov, "Engineering of low-loss metal for nanoplasmonic and metamaterials applications," *Appl. Phys. Lett.*, vol. 95, pp. 151 102 – 151 102–3, 2009.

[18] V. P. Drachev, U. K. Chettiar, A. V. Kildishev, H.-K. Yuan, W. Cai, and V. M. Shalaev, "The ag dielectric function in plasmonic metamaterials," *Optics express*, vol. 16, no. 2, pp. 1186–1195, 2008.

[19] P. B. Johnson and R. Christy, "Optical constants of the noble metals," *Phys. Rev. B*, vol. 6, p. 4370, 1972.

[20] V. M. Shalaev, "Transforming light," *Sci.*, vol. 322, no. 5900, pp. 384–386, 2008.

[21] A. A. Maradudin, J. R. Sambles, and W. L. Barnes, *Modern Plasmonics*. Elsevier, 2014.

[22] A. Boltasseva and H. A. Atwater, "Low-loss plasmonic metamaterials," *Science*, 2011.

[23] J. B. Khurgin and A. Boltasseva, "Reflecting upon the losses in plasmonics and metamaterials," *MRS Bull.*, vol. 37, pp. 768–779, 2012.

[24] G. V. Naik, J. Kim, and A. Boltasseva, "Oxides and nitrides as alternative plasmonic materials in the optical range," *Opt. Mater. Exp.*, vol. 1, no. 6, pp. 1090–1099, 2011.

[25] D. S. Ginley and C. Bright, "Transparent conducting oxides," *Mrs Bulletin*, vol. 25, no. 08, pp. 15–18, 2000.

[26] T. Minami, "New n-type transparent conducting oxides," *Mrs Bulletin*, vol. 25, no. 08, pp. 38–44, 2000.

[27] B. G. Lewis and D. C. Paine, "Applications and processing of transparent conducting oxides," *Mrs Bulletin*, vol. 25, no. 08, pp. 22–27, 2000.

[28] R. B. H. Tahar, T. Ban, Y. Ohya, and Y. Takahashi, "Tin doped indium oxide thin films: Electrical properties," *Journal of Applied Physics*, vol. 83, no. 5, pp. 2631–2645, 1998.

[29] D. B. Chrisey and G. K. Hubler, "Pulsed laser deposition of thin films," *Pulsed Laser Deposition of Thin Films, by Douglas B. Chrisey (Editor), Graham K. Hubler (Editor), pp. 648. ISBN 0-471-59218-8. Wiley-VCH, May 2003.*, vol. 1, 2003.

[30] M. Dressel, *Electrodynamics of solids: optical properties of electrons in matter*. Cambridge University Press, 2002.

[31] P. Drude, "Zur elektronentheorie der metalle," *Annalen der Physik*, vol. 306, no. 3, pp. 566–613, 1900.

[32] C. Kittel and P. McEuen, *Introduction to solid state physics*. Wiley New York, 1976, vol. 8.

[33] M. Yoon, S. Lee, H. Park, H. Kim, and M. Jang, "Solid solubility limits of Ga and Al in ZnO," *Journal of materials science letters*, vol. 21, no. 21, pp. 1703–1704, 2002.

[34] P. Barquinha, A. Pimentel, A. Marques, L. Pereira, R. Martins, and E. Fortunato, "Influence of the semiconductor thickness on the electrical properties of transparent tfts based on indium zinc oxide," *Journal of non-crystalline solids*, vol. 352, no. 9, pp. 1749–1752, 2006.

[35] J. Kim, G. V. Naik, N. Emani, U. Guler, and A. Boltasseva, "Plasmonic resonances in nanostructured transparent conducting oxide films," *IEEE J. Sel. Top. Quant. Electron.*, vol. 19, p. 4601907, 2013.

[36] C. Rhodes, S. Franzen, J. P. Maria, M. Losego, D. N. Leonard, B. Laughlin, G. Duscher, and S. Weibel, "Surface plasmon resonance in conducting metal oxides," *J. Appl. Phys.*, vol. 100, p. 054905, 2006.

[37] M. A. Noginov, L. Gu, J. Livenere, G. Zhu, A. K. Pradhan, R. Mundle, M. Bahoura, Y. A. Barnakov, and V. A. Podolskiy, "Transparent conductive oxides: Plasmonic materials for telecom wavelengths," *Appl. Phys. Lett.*, vol. 99, p. 021101, 2011.

[38] A. V. Kildishev and V. M. Shalaev, "Engineering space for light via transformation optics," *Optics letters*, vol. 33, no. 1, pp. 43–45, 2008.

[39] J. H. Noh, H. S. Jung, J.-K. Lee, J. Y. Kim, C. M. Cho, J.-S. An, and K. S. Hong, "Reversible change in electrical and optical properties in epitaxially grown Al-doped ZnO thin films," *Appl. Phys. Lett.*, vol. 104, p. 073706, 2008.

[40] H. Kim, J. Horwitz, S. Qadri, and D. Chrisey, "Epitaxial growth of al-doped zno thin films grown by pulsed laser deposition," *Thin Solid Films*, vol. 420, pp. 107–111, 2002.

[41] G. Dresselhaus, "Optical absorption band edge in anisotropic crystals," *Phys. Rev.*, vol. 105, pp. 135–138, 1957.

[42] Y. Kajikawa, "Texture development of non-epitaxial polycrystalline zno films," *J. Cryst. Growth*, vol. 289, no. 1, pp. 387 – 394, 2006.

[43] R. M. Martin, *Electronic Structure. Basic Theory and Practical Methods*. New York: Cambridge University Press, 2004.

[44] V. I. Gavrilenko, *Optics of Nanomaterials*. Singapore: Pan Stanford Publishing, 2011.

[45] V. I. Gavrilenko and F. Bechstedt, "Optical functions of semiconductors beyond density functional theory," *Phys. Rev. B*, vol. 55, p. 4343, 1997.

[46] P. Gori, M. Rakel, C. Cobert, W. Richter, N. Esser, A. Hoffmann, R. D. Sole, A. Cricenti, and O. Pulci, "Optical spectra of ZnO in the far ultraviolet: First-principles calculations and ellipsometric measurements," *Phys. Rev. B*, vol. 81, p. 125201, 2010.

[47] X. M. Duan, C. Stampfl, M. M. M. Bilek, and D. R. McKenzie, "Codoping of aluminum and galium with nitrogen in zno: A comparative first-principles investigation," *Phys. Rev. B*, vol. 79, p. 235208, 2009.

[48] A. R. H. Preston, B. J. Ruck, L. F. J. Piper, A. DeMasi, K. E. Smith, A. Schleife, F. Fuchs, F. Bechstedt, J. Chai, and S. M. Durbin, "Band structure of zno from resonant x-ray emission spectroscopy," *Phys. Rev. B*, vol. 78, p. 155114, 2008.

[49] J. G. E. Jellison and L. A. Boatner, "Optical functions of uniaxial ZnO determined by generalized ellipsometry," *Phys. Rev. B*, vol. 58, p. 3586, 1998.

[50] J. F. Muth, R. M. Kolbas, A. K. Sharma, S. Oktyabrsky, and J. Narayan, "Excitonic structure and absorption coefficient measurements of ZnO single crystal epitaxial films deposited by pulsed laser deposition," *J. Appl. Phys.*, vol. 85, p. 7884, 1999.

[51] E. Burstein, "Anoma1ous optical absorption limit in InSb," *Phys. Rev.*, vol. 93, p. 632, 1954.

[52] V. I. Gavrilenko, "Optics of nanostructured materials from first principles," in *Tutorials in Complex Photonic Media*, M. A. Noginov, M. W. McCall, G. Dewar, and N. I. Zheludev, Eds. Bellingham: SPIE Press, 2009, ch. 15, pp. 479–524.

[53] I. Vurgaftman, J. R. Meyer, and L. R. Ram-Mohan, "Band parameters for IIIV compound semiconductors and their alloys," *J. Appl. Phys.*, vol. 89, p. 5815, 2002.

[54] M. Yamaga, E. G. Víllora, K. Shimamura, N. Ichinose, and M. Honda, "Donor structure and electric transport mechanism in $\beta - Ga_2O_3$," *Phys. Rev. B*, vol. 155, p. 155207, 2003.

[55] Y. Zhang, J. Yan, G. Zhao, and W. Xie, "First-principles study on electronic structure and optical properties of Sn-doped $\beta - Ga_2O_3$," *Physica B*, vol. 405, p. 3899, 2010.

[56] N. Liu, M. L. Tang, M. Hentschel, H. Giessen, and A. P. Alivisatos, "Nanoantenna-enhanced gas sensing in a single tailored nanofocus," *Nature materials*, vol. 10, no. 8, pp. 631–636, 2011.

[57] E. M. Larsson, C. Langhammer, I. Zorić, and B. Kasemo, "Nanoplasmonic probes of catalytic reactions," *Science*, vol. 326, no. 5956, pp. 1091–1094, 2009.

[58] R. Elghanian, J. J. Storhoff, R. C. Mucic, R. L. Letsinger, and C. A. Mirkin, "Selective colorimetric detection of polynucleotides based on the distance-dependent optical properties of gold nanoparticles," *Science*, vol. 277, no. 5329, pp. 1078–1081, 1997.

[59] F. Le, D. W. Brandl, Y. A. Urzhumov, H. Wang, J. Kundu, N. J. Halas, J. Aizpurua, and P. Nordlander, "Metallic nanoparticle arrays: a common substrate for both surface-enhanced raman scattering and surface-enhanced infrared absorption," *ACS nano*, vol. 2, no. 4, pp. 707–718, 2008.

[60] N. Engheta, "Circuits with light at nanoscales: optical nanocircuits inspired by metamaterials," *Science*, vol. 317, no. 5845, pp. 1698–1702, 2007.

[61] W. Cai and V. M. Shalaev, *Optical metamaterials*. Springer, 2010, vol. 10.

[62] S. Lal, S. Link, and N. J. Halas, "Nano-optics from sensing to waveguiding," *Nature photonics*, vol. 1, no. 11, pp. 641–648, 2007.

[63] G. Garcia, R. Buonsanti, E. L. Runnerstrom, R. J. Mendelsberg, A. Llordes, A. Anders, T. J. Richardson, and D. J. Milliron, "Dynamically modulating the surface plasmon resonance of doped semiconductor nanocrystals," *Nano letters*, vol. 11, no. 10, pp. 4415–4420, 2011.

[64] M. Kanehara, H. Koike, T. Yoshinaga, and T. Teranishi, "Indium tin oxide nanoparticles with compositionally tunable surface plasmon resonance frequencies in the near-ir region," *Journal of the American Chemical Society*, vol. 131, no. 49, pp. 17 736–17 737, 2009.

[65] B. T. Diroll, T. R. Gordon, E. A. Gaulding, D. R. Klein, T. Paik, H. J. Yun, E. Goodwin, D. Damodhar, C. R. Kagan, and C. B. Murray, "Synthesis of n-type plasmonic oxide nanocrystals and the optical and electrical characterization of their transparent conducting films," *Chemistry of Materials*, 2014.

[66] T. R. Gordon, T. Paik, D. R. Klein, G. V. Naik, H. Caglayan, A. Boltasseva, and C. B. Murray, "Shape dependent plasmonic response and directed self assembly in a new semiconductor building block, indium doped cadmium oxide (ico)," *Nano lett.*, 2013.

[67] S. Q. Li, P. Guo, L. Zhang, W. Zhou, T. W. Odom, T. Seideman, J. B. Ketterson, and R. P. Chang, "Infrared plasmonics with indium–tin-oxide nanorod arrays," *ACS nano*, vol. 5, no. 11, pp. 9161–9170, 2011.

[68] S.-Q. Li, P. Guo, D. B. Buchholz, W. Zhou, Y. Hua, T. W. Odom, J. Ketterson, L. E. Ocola, K. Sakoda, and R. P. Chang, "Plasmonic–photonic mode coupling in indium-tin-oxide nanorod arrays," *ACS Photonics*, vol. 1, no. 3, pp. 163–172, 2014.

[69] Y. B. Zheng, B. K. Juluri, X. Mao, T. R. Walker, and T. J. Huang, "Systematic investigation of localized surface plasmon resonance of long-range ordered au nanodisk arrays," *Journal of Applied Physics*, vol. 103, no. 1, p. 014308, 2008.

[70] T. Rindzevicius, Y. Alaverdyan, M. Käll, W. A. Murray, and W. L. Barnes, "Long-range refractive index sensing using plasmonic nanostructures," *The Journal of Physical Chemistry C*, vol. 111, no. 32, pp. 11 806–11 810, 2007.

[71] C. Langhammer, M. Schwind, B. Kasemo, and I. Zoric, "Localized surface plasmon resonances in aluminum nanodisks," *Nano letters*, vol. 8, no. 5, pp. 1461–1471, 2008.

[72] C. Langhammer, Z. Yuan, I. Zoric, and B. Kasemo, "Plasmonic properties of supported pt and pd nanostructures," *Nano letters*, vol. 6, no. 4, pp. 833–838, 2006.

[73] H. Caglayan, S.-H. Hong, B. Edwards, C. R. Kagan, and N. Engheta, "Near-infrared metatronic nanocircuits by design," *Physical review letters*, vol. 111, no. 7, p. 073904, 2013.

[74] M. Abb, Y. Wang, N. Papasimakis, C. H. de Groot, and O. L. Muskens, "Surface-enhanced infrared spectroscopy using metal oxide plasmonic antenna arrays," *Nano Letters*, vol. 14, no. 1, pp. 346–352, 2014, pMID: 24341902.

[75] S. Pennycook, "Z-contrast stem for materials science," *Ultramicroscopy*, vol. 30, no. 1, pp. 58–69, 1989.

[76] T. Wang, M. Zalkovskij, K. Iwaszczuk, A. V. Lavrinenko, G. V. Naik, J. Kim, A. Boltasseva, and P. U. Jepsen, "Ultrabroadband terahertz conductivity of highly doped zno and ito," *Optical Materials Express*, vol. 5, no. 3, pp. 566–575, 2015.

[77] T. Søndergaard, J. Jung, S. I. Bozhevolnyi, and G. Della Valle, "Theoretical analysis of gold nano-strip gap plasmon resonators," *New Journal of Physics*, vol. 10, no. 10, p. 105008, 2008.

[78] J. Jung, T. Søndergaard, and S. I. Bozhevolnyi, "Gap plasmon-polariton nanoresonators: Scattering enhancement and launching of surface plasmon polaritons," *Physical Review B*, vol. 79, no. 3, p. 035401, 2009.

[79] D. Lin-Vien, N. B. Colthup, W. G. Fateley, and J. G. Grasselli, *The handbook of infrared and Raman characteristic frequencies of organic molecules*. Elsevier, 1991.

[80] M. J. Tarlov, "Silver metalization of octadecanethiol monolayers self-assembled on gold," *Langmuir*, vol. 8, no. 1, pp. 80–89, 1992.

[81] A. V. Kildishev, A. Boltasseva, and V. M. Shalaev, "Planar photonics with metasurfaces," *Science*, vol. 339, no. 6125, p. 1232009, 2013.

[82] L. Huang, X. Chen, H. Mühlenbernd, H. Zhang, S. Chen, B. Bai, Q. Tan, G. Jin, K.-W. Cheah, C.-W. Qiu *et al.*, "Three-dimensional optical holography using a plasmonic metasurface," *Nature communications*, vol. 4, 2013.

[83] Y. Montelongo, J. O. Tenorio-Pearl, C. Williams, S. Zhang, W. I. Milne, and T. D. Wilkinson, "Plasmonic nanoparticle scattering for color holograms," *Proceedings of the National Academy of Sciences*, vol. 111, no. 35, pp. 12 679–12 683, 2014.

[84] X. Chen, L. Huang, H. Mühlenbernd, G. Li, B. Bai, Q. Tan, G. Jin, C.-W. Qiu, S. Zhang, and T. Zentgraf, "Dual-polarity plasmonic metalens for visible light," *Nature communications*, vol. 3, p. 1198, 2012.

[85] F. Aieta, P. Genevet, M. A. Kats, N. Yu, R. Blanchard, Z. Gaburro, and F. Capasso, "Aberration-free ultrathin flat lenses and axicons at telecom wavelengths based on plasmonic metasurfaces," *Nano letters*, vol. 12, no. 9, pp. 4932–4936, 2012.

[86] M. Kim, A. M. Wong, and G. V. Eleftheriades, "Optical huygens metasurfaces with independent control of the magnitude and phase of the local reflection coefficients," *Physical Review X*, vol. 4, no. 4, p. 041042, 2014.

[87] A. Pors, O. Albrektsen, I. P. Radko, and S. I. Bozhevolnyi, "Gap plasmon-based metasurfaces for total control of reflected light," *Scientific reports*, vol. 3, 2013.

[88] N. Yu, F. Aieta, P. Genevet, M. A. Kats, Z. Gaburro, and F. Capasso, "A broadband, background-free quarter-wave plate based on plasmonic metasurfaces," *Nano letters*, vol. 12, no. 12, pp. 6328–6333, 2012.

[89] A. Roberts and L. Lin, "Plasmonic quarter-wave plate," *Optics letters*, vol. 37, no. 11, pp. 1820–1822, 2012.

[90] J. K. Gansel, M. Thiel, M. S. Rill, M. Decker, K. Bade, V. Saile, G. von Freymann, S. Linden, and M. Wegener, "Gold helix photonic metamaterial as broadband circular polarizer," *Science*, vol. 325, no. 5947, pp. 1513–1515, 2009.

[91] A. Shaltout, J. Liu, A. Kildishev, and V. Shalaev, "Photonic spin hall effect in gap–plasmon metasurfaces for on-chip chiroptical spectroscopy," *Optica*, vol. 2, no. 10, pp. 860–863, 2015.

[92] E. H. Khoo, E. P. Li, and K. B. Crozier, "Plasmonic wave plate based on subwavelength nanoslits," *Optics letters*, vol. 36, no. 13, pp. 2498–2500, 2011.

[93] Y. Zhao and A. Alu, "Tailoring the dispersion of plasmonic nanorods to realize broadband optical meta-waveplates," *Nano letters*, vol. 13, no. 3, pp. 1086–1091, 2013.

[94] B. Edwards, A. Alù, M. E. Young, M. Silveirinha, and N. Engheta, "Experimental verification of epsilon-near-zero metamaterial coupling and energy squeezing using a microwave waveguide," *Physical Review Letters*, vol. 100, no. 3, p. 033903, 2008.

[95] A. Alù and N. Engheta, "Light squeezing through arbitrarily shaped plasmonic channels and sharp bends," *Physical Review B*, vol. 78, no. 3, p. 035440, 2008.

[96] D. Adams, S. Inampudi, T. Ribaudo, D. Slocum, S. Vangala, N. Kuhta, W. Goodhue, V. Podolskiy, and D. Wasserman, "Funneling light through a subwavelength aperture with epsilon-near-zero materials," *Physical review letters*, vol. 107, no. 13, p. 133901, 2011.

[97] R. W. Ziolkowski, "Propagation in and scattering from a matched metamaterial having a zero index of refraction," *Physical Review E*, vol. 70, no. 4, p. 046608, 2004.

[98] A. Alù and N. Engheta, "Antenna matching in ε-near-zero metamaterial channels," in *Antenna Technology, 2009. iWAT 2009. IEEE International Workshop on*. IEEE, 2009, pp. 1–4.

[99] M. Silveirinha and N. Engheta, "Tunneling of electromagnetic energy through subwavelength channels and bends using ε-near-zero materials," *Physical review letters*, vol. 97, no. 15, p. 157403, 2006.

[100] R. Maas, J. Parsons, N. Engheta, and A. Polman, "Experimental realization of an epsilon-near-zero metamaterial at visible wavelengths," *Nature Photonics*, 2013.

[101] D. Traviss, R. Bruck, B. Mills, M. Abb, and O. L. Muskens, "Ultrafast plasmonics using transparent conductive oxide hybrids in the epsilon-near-zero regime," *Applied Physics Letters*, vol. 102, no. 12, p. 121112, 2013.

[102] N. Engheta, C. Papas, and C. Elachi, "Radiation patterns of interfacial dipole antennas," *Radio Science*, vol. 17, no. 6, pp. 1557–1566, 1982.

[103] B. Simpkins, J. Long, O. Glembocki, J. Guo, J. Caldwell, and J. Owrutsky, "Pitch-dependent resonances and near-field coupling in infrared nanoantenna arrays," *Optics express*, vol. 20, no. 25, pp. 27 725–27 739, 2012.

[104] F. Neubrech, T. Kolb, R. Lovrincic, G. Fahsold, A. Pucci, J. Aizpurua, T. Cornelius, M. Toimil-Molares, R. Neumann, and S. Karim, "Resonances of individual metal nanowires in the infrared," *Applied Physics Letters*, vol. 89, no. 25, p. 253104, 2006.

[105] L. Novotny, "Effective wavelength scaling for optical antennas," *Physical Review Letters*, vol. 98, no. 26, p. 266802, 2007.

VITA

VITA

Jongbum Kim received the B.E. degree in Electrical and Computer Engineering from Korea University, Korea in 2007. He is currently working toward a Ph.D. degree in the Department of Electrical Engineering at Purdue University. His research interests include fabrication of devices for plasmonics and metamaterials based on transparent conducting oxides (TCOs).

Jongbum Kim's publications from his research at Purdue University in reverse chronological order are:

Journal Articles during Ph.D

[12] Z. Zhang, F. Zuo, C. Wan, A. Datta, Jongbum Kim, J. Rensberg, R. Nawrodt, H. Park, T. Larrabee, X. Guan, Y. Zhou, S.M. Prokes, C. Ronning, V. M. Shalaev, A. Boltasseva, M. Kats, and S. Ramanathan, Evolution of metallicity in vanadium dioxide by creation of oxygen vacancies Under review on Advanced Optical Materials

[11] U. Guler, D. Zemlyanov, Jongbum Kim, Z. Wang, R. Chandrasekar, X. Meng, E. Stach, A. V. Kildishev, A. Boltasseva, and V. M. Shalaev, Plasmonic Titanium Nitride Nanostructures via Nitridation of Titanium Oxide Under review on Advanced Optical Materials

[10] Jongbum Kim, S. Choudhary, C. DeVault, Y. Zhao, A. V. Kildishev, V. M. Shalaev A. Alu and A. Boltasseva, Controlling the Polarization state of Light with Plasmonic Metal Oxide Metasurfaces ACS Nano, vol.10, no 10, pp. 93269333, 2016

[9] A. M. Shaltout*, N. Kinsey*, Jongbum Kim*, R. Chandrasekar*, J. C. Ndukaife*, A. Boltasseva, and V. M. Shalaev Development of Optical Metasurfaces: Emerging Concepts and New Materials" Proceeding of the IEEE, vol PP, no. 99, pp.1-18, 2016 (* Co-leading authors)

[8] L. Caspani, R. P. M. Kaipurath, M. Clerici, M. Ferrera, T. Roger, A. Di Falco, Jongbum Kim, N. Kinsey, V. M. Shalaev, A. Boltasseva, and D. Faccio Enhanced Nonlinear Refractive Index in Epsilon-Near-Zero Materials Physical Review Letters, vol. 116, pp. 233901, 2016

[7] Jongbum Kim, A. Dutta, G. V. Naik, A. V. Kildishev, A. Giles, F. J. Bezares, O. J. Glembocki, A. Mahmoud, H. Caglayan, J. D. Caldwell, A. Boltasseva, and N. Engheta, The Role of Epsilon-Near-Zero Substrates in the Optical Response of Plasmonic Antennas Optica, vol. 3, no. 3, pp. 339-346, 2016

[6] Jongbum Kim, A. Dutta, B. Memarzadeh, A. V. Kildishev, H. Mosallaei, and A. Boltasseva, Zinc Oxide Based Plasmonic Multilayer Resonator: Localized and Gap Surface Plasmon in the Infrared." ACS Photonics, vol. 3, no. 8, pp. 1224-1230, 2015

[5] N. Kinsey, C. DeVault, Jongbum Kim, M. Ferrera, V. M. Shalaev, and A. Boltas-

seva, Epsilon-Near-Zero Al-doped ZnO for Ultrafast Switching at Telecom Wavelengths." Optica, vol. 2, no. 7, pp. 616-622, 2015 (Cover letter)

[4] W. Tianwu, M. Zalkovskij, K. Iwaszczuk, A. V. Lavrinenko, G. V. Naik, Jongbum Kim, A. Boltasseva, and P. U. Jepsen, Ultrabroadband Terahertz Conductivity of Highly Doped ZnO and ITO." Optical Materials Express, vol. 5, no. 3, pp. 566-575, 2015

[3] Jongbum Kim, G. V. Naik, A. V. Gavrilenko, K. Dondapati, V. I. Gavrilenko, S.M. Prokes, O. J. Glembocki, V. M. Shalaev, and A. Boltasseva, Optical Properties of Gallium-Doped Zinc Oxide-A Low-Loss Plasmonic Material: First-Principles Theory and Experiment.", Physical Review X, vol. 3, no. 4, pp. 041037, 2013 (Invited letter) [2] Jongbum Kim, G. V. Naik, N. K. Emani, U. Guler, and A. Boltasseva, Plasmonic Resonances in Nanostructured Transparent Conducting Oxide Films," Selected Topics in Quantum Electronics, IEEE Journal of, vol.19, no. 3, pp.4601907, 2013 (Invited letter) (Cover letter)

[1] G. V. Naik, Jongbum Kim, and A. Boltasseva, Oxides and Nitrides as Alternative Plasmonic Materials in the Optical Range" Optical Materials Express, vol. 1, no. 6, pp. 1090-1099, 2011 (Invited letter)

Book Chapter during Ph.D

[1] G. V. Naik, Jongbum Kim, N. Kinsey, A. Boltasseva, Alternative plasmonic materials, Chapter in "Modern Plasmonics" Eds: A. A. Maradudin, J. R. Sambles and W. L. Barnes, Elsevier, Sep. 2014

Conference during Ph.D

[13] C. DeVault, N. Kinsey, Jongbum Kim, A. Dutta, M. Ferrera, V. M. Shalaev, and A. Boltasseva, "Ultrafast Optical Tuning of Epsilon-Near-Zero Thin Films," in Conference on Lasers and Electro-Optics (CLEO), San Jose, CA, USA, Jun 2016

[12] A. Shaltout*, Jongbum Kim*, A. Kildishev, A. Boltasseva, and V. M. Shalaev,

"Implementation of Metasurface Based Nano-Cavities," in Conference on Lasers and Electro-Optics (CLEO), San Jose, CA, USA, Jun 2016 (* Co-leading authors)

[11] Jongbum Kim, N. Kinsey, A. Dutta, M. Ferrera, C. DeVault, A. V. Kildishev, V. M. Shalaev and A. Boltasseva, "Transparent conducting oxides as plasmonic component in near infrared", in SPIE Nanoscience+ Engineering, International Society for Optics and Photonics, San Diego, CA, USA, Oct 2015

[10] N. Kinsey, C. DeVault, Jongbum Kim, M. Ferrera, A. V. Kildishev, V. M. Shalaev and A. Boltasseva, Ultrafast dynamics of Al-doped zinc oxide under optical excitation", in SPIE Nanoscience+ Engineering, International Society for Optics and Photonics, San Diego, CA, USA, Oct 2015

[9] N. Kinsey, M. Ferrera, C. DeVault, Jongbum Kim, A. V. Kildishev, V. M. Shalaev and A. Boltasseva, Alternative materials lead to practical nanophotonic components", in SPIE Nanoscience+ Engineering, International Society for Optics and Photonics, San Diego, CA, USA, Oct 2015

[8] N. Kinsey, M. Ferrera, C. DeVault, Jongbum Kim, A. Dutta, K. Chaudhuri, S. Choudhuri, V. M. Shalaev, and A. Boltasseva, Practical Platform for Nanophotonics with Refractory Plasmonic Metal Nitrides and Transparent Conducting Oxides", in Frontiers in Optics Proceedings, San Jose, CA, USA, Oct 2015

[7] Jongbum Kim, A. Dutta, G. V. Naik, A. V. Kildishev, A. Boltasseva, A. Giles, F. J. Bezares, O. J. Glembocki, J. D. Caldwell, A. Mahmoud, H. Caglayan, and N. Engheta, Gold Antenna on Epsilon-near-Zero Substrates: Effect on Radiation Pattern and Resonance Frequency in MRS Spring meeting 2015, San Francisco, CA, USA, Apr 2015

[6] N. Kinsey, U. Guler, Jongbum Kim, G. V. Naik, V. M. Shalaev, and A. Boltasseva, "Developing ceramic materials for practical plasmonics," in SPIE Nanoscience+ Engineering, International Society for Optics and Photonics, San Diego, CA, USA, Aug 2014

[5] Jongbum Kim, Y. Zhao, A. Dutta, S. M. Choudhury, A. Kildishev, A. Alu, and A. Boltasseva, "Nanostructured Transparent Conducting Oxide Films for Polarization Control with Plasmonic Metasurfaces", in Conference on Lasers and Electro-Optics (CLEO), San Jose, CA, USA, Jun 2014

[4] Jongbum Kim, B. Memarzadeh, A. Dutta, S. M. Choudhury, A. Kildishev, H. Mosallaei, and A. Boltasseva, "GZO/ZnO Multilayered nanodisk metasurface to engineer the plasma frequency", in Conference on Lasers and Electro-Optics (CLEO), San Jose, CA, USA, Jun 2014

[3] Jongbum Kim, Y. Zhao, G. V. Naik, N. K. Emani, U. Guler, A. Kildishev, A. Alu, and A. Boltasseva, "Nanostructured Transparent Conductive Oxide Films for Plasmonic Applications", in Conference on Lasers and Electro-Optics (CLEO), San Jose, CA, USA, Jun 2013

[2] G. V. Naik, Jongbum Kim, U. Giler, N. K. Emani, P. R. West, N. Kinsey, J. S. Ndukaife and A. Boltasseva, "Empowering plasmonics and metamaterials technology with new material platforms", in Proceedings of V Intnl. Conf. Frontiers of Nonlinear Physics, Nizhny Novgorod, Russia, 2013

[1] A. V. Gavrilenko, K. Dondapati, V. I. Gavrilenko, Jongbum Kim, G. V. Naik, A. Boltasseva, "Optical functions of nano-crystalline ZnO containing voids and doped with Ga", in SPIE Nanoscience+ Engineering, International Society for Optics and Photonics, San Diego, CA, USA, Oct 2012